Nonlinear Dynamics (2026) 114:266
https://doi.org/10.1007/s11071-025-12212-x

RESEARCH

Instability of a moving mass suspended electromagnetically from a periodically supported beam at high speed

Rens J. van Leijden[1] · Karel N. van Dalen[1] · Andrei B. Fărăgău[1] · Jithu Paul[1] · Andrei V. Metrikine[1]

Received: 4 August 2025 / Revised: 23 December 2025 / Accepted: 30 December 2025

Abstract

This study addresses the dynamic stability of a moving mass suspended electromagnetically from a flexible beam that is supported periodically by discrete elastic springs. The stability is generally determined by the interaction of the wave-induced and electromagnetic instability mechanisms. Both are related to a potentially destabilizing force: the controlled electromagnetic force and the reaction force of the guideway (beam-foundation system). The former is destabilizing if the control is inappropriate, and the latter when sufficiently energetic anomalous Doppler waves are excited in the guideway that feedback energy into the vehicle vibration. Using a generalization of Hill's method, the stability boundary is determined in the plane of electromagnetic-control parameters. The obtained boundary is roughly triangular, like for the equivalent non-periodic system. The left, straight boundary marks the emergence of a divergence instability. The right boundary generally marks the emergence of an oscillatory (flutter-type) instability, but specific, elliptical indentations are related to parametric resonances. The divergence instability is always electromagnetics induced, but the oscillatory instability and parametric resonances can be either wave or electromagnetics induced, although the latter are often electromagnetics induced. Wave-induced instability takes place mostly for large speeds and only for small values of the control parameters. The stability boundary locally bends back there, reducing the size of the stable zone considerably. Next to the T and $2T$ parametric-resonance indentations, the right boundary has a significant amorphous indentation compared to that of the non-periodic system. Furthermore, the $2T$ parametric resonance ellipse is very significant in size when the inhomogeneity of the periodic guideway is relatively strong. Interestingly, the amorphous indentation is related to the occurrence of an evanescent wave in the periodic guideway, but parametric resonance appears to be not uniquely related to a single wave type. Although the current study is fundamental in nature, the findings do pave the way towards the design of safe and cost-effective Maglev and Hyperloop infrastructure as well as of electromagnetic-suspension controllers. We emphasize that the wave-induced instability mechanism, and more generally speaking the influence of the periodic guideway, is also relevant in the context of other (than the simple PD) control strategies as well as for different Maglev and Hyperloop suspension/levitation systems such as the electrodynamic, the hybrid and the superconducting magnet suspensions.

Keywords Electromagnetically suspended mass · Periodically supported beam · Interaction of instability mechanisms at high speed · Anomalous Doppler waves · Maglev & Hyperloop

Rens J. van Leijden and Karel N. van Dalen have contributed equally to this work

✉ Karel N. van Dalen
k.n.vandalen@tudelft.nl

Rens J. van Leijden
rens@delft-cymatics.com

Andrei B. Fărăgău
a.b.faragau@tudelft.nl

Jithu Paul
jithupaulv@gmail.com

Andrei V. Metrikine
a.metrikine@tudelft.nl

[1] Department of Engineering Structures, Delft University of Technology, Mekelweg 5, 2628 Delft, CD, The Netherlands

Published online: 24 February 2026

1 Introduction

Hyperloop is a potential new transportation mode that is currently under development [1–4]. Maglev technology is advancing at the same time [5–9]. The very high target speeds of the guided vehicles pose a unique challenge regarding the stability of the vibration of the vehicle and the guideway. For vehicle suspensions involving an electromagnet, the vehicle-guideway system stability is essentially determined by the interaction of three potentially destabilizing state-dependent forces: the *electromagnetic force*, the *aeroelastic force*, and the *reaction force of the flexible guideway*. Thorough understanding of this interaction is paramount for the effective design of the infrastructure, which is one of the most costly elements of the Maglev and Hyperloop systems [1, 4, 10, 11]; the infrastructure should be lightweight to cut costs, but safety and comfort should be guaranteed.

The electromagnetic suspension force is inherently unstable and needs to be controlled. When the control is chosen properly, the stability of an electromagnetically suspended mass can in principle be guaranteed [5, 7, 12–15]; assessment of the *electromagnetic instability mechanism* for high-speed Maglev vehicles in several studies [e.g.,5, 7, 11]. It is also well-known that the aeroelastic force acting on a moving object can be destabilizing depending on the change of the aeroelastic coefficients with the angle of attack [16]; assessment of the *aeroelastic instability mechanism* for moving high-speed vehicles has been done in numerous studies [e.g.,17]. The least well-known is that instability can be induced by the reaction force of a flexible guideway. Early studies considering a mass moving on a beam supported by a distributed elastic foundation showed that the critical speed beyond which the vibrations of the mass-beam system become unstable is the minimum phase velocity of waves in the beam (the critical speed is larger if the foundation includes damping); the beam's reaction force then feeds back the energy of excited so-called anomalous Doppler waves into the vehicle vibration [18–20]. More comprehensive models assessed the importance of this *wave-induced instability mechanism* for conventional and high-speed guided transportation modes [21–25].

The separate instability mechanisms have been investigated in quite some detail, and it is more or less known when to expect stability problems. However, the interaction of the instability mechanisms has only been investigated to a limited extent. Different aspects of the interaction of the electromagnetic and aeroelastic forces have been addressed [15, 26–28]; the aeroelastic load essentially changes the system characteristics (i.e., the damping) of a high-speed Maglev train, which may lead to a self-excited vibration when the control of the electromagnetic force accounts insufficiently for this change in the system [27]. The interaction of the electromagnetic and guideway's reaction forces has still many open questions; the current paper addresses some of those.

Studies into vehicle-structure interaction for (electro) magnetically levitated/suspended vehicles either typically consider guideways of finite length [11, 13, 29–34] or apply the concept of moving system boundaries to mimic an infinite guideway [14, 35]. In such models, the wave-induced instability mechanism can either not occur at all or will be disturbed by entrance and exit effects of the moving vehicle. The models are therefore inappropriate or not well suited for studying the interaction of the wave-induced and the electromagnetic instability mechanisms. The first studies into this interaction considered the model of a moving mass suspended electromagnetically from an infinite beam, which is supported by a distributed foundation having constant support stiffness and damping (i.e., a Winkler-type foundation) [36, 37]. Results show that when the control system is properly tuned, ensuring the electromagnetic force has a stabilizing character at small speed, the critical speed beyond which the vibrations of the vehicle and guideway can become unstable is larger than the minimum phase velocity of waves in the beam (like for moving-mass-on-beam-with-damping problem addressed above [19]). In many situations, the energy input by the guideway's reaction force cannot be dissipated by the (controlled) electromagnetic force; in other words, the stable domain shrinks drastically in size above the critical speed.

The assumption of distributed constant support stiffness adopted by Fărăgău et al. [37] is in fact a simplification, and the question is at what speed the vibration becomes unstable if the periodic character of the foundation is accounted for; Maglev and Hyperloop infrastructures are typically supported by periodically placed piers. Studies into purely mechanical systems show that instability due to parametric resonance can occur at relatively small speed when the support conditions are periodic, both for discrete (i.e., consisting of localized springs) and non-discrete foundations [22, 38–41]. The current study therefore addresses the stability of a moving mass suspended electromagnetically from a beam that is supported periodically by discrete elastic springs, thus incorporating both the reaction force of the *periodically* supported beam (unlike Ref. [37], where the support stiffness was considered constant) as well as the electromagnetic force.

This paper contains a comprehensive stability analysis and reveals several instability types for the considered system – divergence, oscillatory (i.e., flutter-type) instability and parametric resonance – and discusses their importance; early studies already indicated their existence for magnetically levitated objects/vehicles (the so-called EDS system) subject to an oscillating base or in contact with a flexible guideway [10, 42, 43]. Furthermore, the relation between the instability types and the underlying instability mecha-

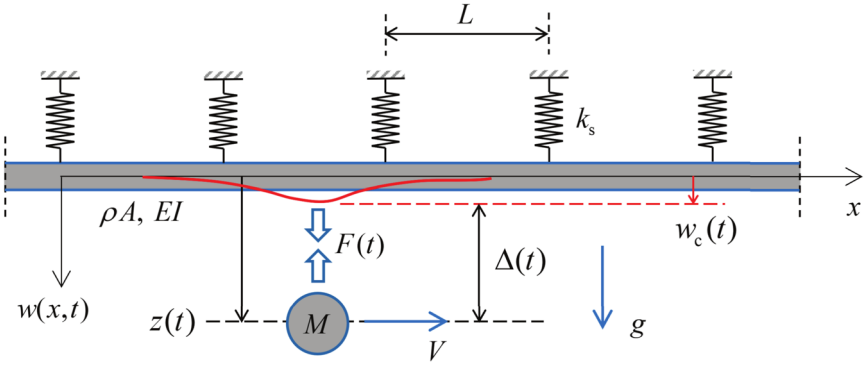

Fig. 1 Model of a moving mass suspended electromagnetically from an infinite Euler-Bernoulli beam that is supported by discrete, periodic springs. The solid red line indicates an arbitrary deflection shape of the beam, which is relevant for the definition of the air gap $\Delta(t)$

nisms (wave-induced, electromagnetic) is addressed using an energy analysis that identifies which of the forces is destabilizing along different parts of the stability boundary [37]. The paper clarifies how the stability is modified by the periodic nature of the foundation through comparison of the obtained results with those of the continuously supported beam with constant stiffness [37], and relates the differences to the wave dynamics beam-foundation system. All in all, the paper paves the way towards design of lightweight and safe Maglev and Hyperloop infrastructure.

It is important to note that the current paper is different from rather recent works on parametric resonance of beams excited by periodically passing moving oscillators/masses [44–46]. Those studies consider finite beams with a large or infinite number of passing objects. The current study is not only different in the definition of the contact force (i.e., electromagnetic instead of viscoelastic or inertial), the difference is more fundamental; it considers a single moving mass that continuously interacts with an infinite beam that has infinitely many periodic supports.

The paper is organized as follows. Section 2 presents the problem statement, including the governing equations. Section 3 addresses the steady-state response of the considered system. Then, Sect. 4 contains the linearized equations (about the steady-state response) for the stability analysis, and the way to find the stability boundary is presented in Sect. 5. Equations for the energy analysis are presented in Sect. 6. Results are shown and discussed in Sect. 7. Section 8 contains the conclusions of the paper.

2 Problem statement

In the paper, we investigate the stability of the free vibration about the steady-state response observed in the model consisting of a moving mass suspended electromagnetically from an infinite Euler-Bernoulli beam that is supported by discrete, periodic springs; see Fig. 1. The moving mass M has (prescribed) constant translational velocity/speed V, and its vertical position is denoted $z(t)$. The beam has mass per unit of length ρA and bending stiffness EI, while k_s is the stiffness of the discrete foundation springs and L is their spacing. $w(x,t)$ is the deflection of the beam, where x denotes the longitudinal coordinate of a non-moving reference system, and t denotes time. The electromagnetic interaction force, which is modeled as a (moving) point load, is denoted $F(t)$, and $\Delta(t)$ is the air gap between the beam and the moving mass. The system is subject to the gravity (with constant g), but the self-weight of the beam is ignored (the beam is initially assumed to be perfectly straight) to study the effect of the foundation-stiffness variation in pure form.

The equation of motion of the beam reads as follows:

$$\rho A\frac{\partial^2 w}{\partial t^2}+EI\frac{\partial^4 w}{\partial x^4}+k_s\sum_{n=-\infty}^{\infty}\delta(x-nL)w = F(t)\delta(x-Vt), \tag{1}$$

where $\delta(...)$ is the Dirac delta function; from this point onwards, the time (and space) dependence of the variables is left out for brevity, unless there is a need to keep it for clarity. The equation of motion of the (point) mass is more simple:

$$M\frac{d^2 z}{dt^2}=-F+Mg. \tag{2}$$

The nonlinear electromagnetic interaction force is defined as

$$F=C\frac{I^2}{\Delta^2}, \tag{3}$$

where C is constant that depends on the electromagnet properties [5, 7, 34], $I=I(t)$ is the current of the electromagnet, and $\Delta=z-w_c$ is the air gap; here, $w_c(t)=w(x=Vt,t)$ is the beam's deflection at the contact point (see Fig. 1). The current depends on the voltage $U=U(t)$ applied to the electromagnet as well as on the air gap through Kirchhoff's voltage law [5, 7, 14, 34, 47]:

$$U=RI+\frac{d}{dt}\left(\frac{2C}{\Delta}I\right) \quad \leftrightarrow$$

$$\frac{dI}{dt} + \frac{\Delta}{2C}\left(R - 2C\frac{\dot{\Delta}}{\Delta^2}\right) I = \frac{\Delta}{2C} U. \tag{4}$$

Here, the overdot represents differentiation with respect to time. The voltage consists of a steady-state part $U_{\mathrm{ss}} = U_{\mathrm{ss}}(t)$ (the subscript "ss" stands for steady state) and a transient part which is activated by the PD controller as soon as the actual air gap and/or its time derivative start to differ from the desired steady-state counterparts (defined in Sect. 3):

$$U = U_{\mathrm{ss}} + K_{\mathrm{p}}\left(\Delta - \Delta_{\mathrm{ss}}\right) + K_{\mathrm{d}}\left(\dot{\Delta} - \dot{\Delta}_{\mathrm{ss}}\right). \tag{5}$$

Here, K_{p} and K_{d} are the proportional and derivative gains of the controller. Note that the PD controller operating on the air gap is chosen for simplicity; the objective of the current paper is to investigate the interaction between the wave-induced and electromagnetic instability mechanisms, not advanced control strategies of the electromagnetic force.

3 Steady-state response

The steady-state response is defined as the response of the system subject to the (moving) gravity force Mg (which is the only external force) and is generally time dependent due to the varying support stiffness; this is different from the situation in Fărăgău et al. [37], where the steady-state response is time independent due to the support stiffness being constant in space. Note that the PD controller is not active in the steady state as $\Delta = \Delta_{\mathrm{ss}}$; hence, U in Eq. (4) is equal to U_{ss} (and Eq. (5) is redundant in that situation).

From the equations governing the steady state (i.e., Eqs. (1)-(4)) it is clear that the amount of dependent variables and the amount of equations do not match; the amount of dependent variables is five – w_{ss} (which includes $w_{\mathrm{c,ss}}$), z_{ss}, F_{ss}, I_{ss}, U_{ss} – while the amount of equations is four. Hence, one of the variables has to be chosen, which allows determining the other ones based on that.

From the practical perspective of avoiding vehicle vibrations, the following choice is made:

$$z_{\mathrm{ss}} = \text{constant}. \tag{6}$$

The magnitude of the constant can be chosen based on the desired air gap red (see below). From Eq. (2) it follows that, if z_{ss} is constant, the interaction force is constant too and equal to the gravity force:

$$F_{\mathrm{ss}} = Mg. \tag{7}$$

The beam's deflection at the contact point $w_{\mathrm{c,ss}}$ induced by the moving gravity force can be determined semi-analytically [48, 49] and consists of a constant part and a time-periodic part, where the fundamental frequency is the support-passing frequency associated with the period $T = V/L$:

$$w_{\mathrm{c,ss}}(t) = Mg \sum_{p=-\infty}^{\infty} c_p \mathrm{e}^{\mathrm{i}\omega_p t}, \quad \omega_p = p\frac{2\pi}{T}. \tag{8}$$

Expressions for the coefficients c_p are given in Appendix A. The steady-state current is subsequently determined using Eq. (3):

$$I_{\mathrm{ss}}(t) = \sqrt{\frac{Mg}{C}}\Delta_{\mathrm{ss}}, \quad \Delta_{\mathrm{ss}}(t) = z_{\mathrm{ss}} - w_{\mathrm{c,ss}}(t). \tag{9}$$

Finally, the steady-state voltage is obtained from Eq. (4):

$$U_{\mathrm{ss}} = RI_{\mathrm{ss}} + 2C\frac{d}{dt}\left(\frac{I_{\mathrm{ss}}}{\Delta_{\mathrm{ss}}}\right) = RI_{\mathrm{ss}}. \tag{10}$$

It is important to note that all steady-state variables in the latter equation are time-varying. The term involving the time derivative vanishes as $F_{\mathrm{ss}} = \text{constant}$ (Eq. (7)), which implies that $I_{\mathrm{ss}}^2/\Delta_{\mathrm{ss}}^2 = \text{constant}$ (see Eq. (3)) and hence $I_{\mathrm{ss}}/\Delta_{\mathrm{ss}} = \text{constant}$.

Clearly, to control the magnitude of the (mean of the) steady-state air gap Δ_{ss} for a given system (i.e., mass, bending stiffness, etc.), the magnitude of the steady-state vehicle position z_{ss} should be chosen (see Eq. (9); note that $w_{\mathrm{c,ss}}$ cannot be influenced when the system is given). The steady-state current and voltage needed to enable this steady-state position and air gap follow accordingly using Eqs. (9) and (10).

4 Linearised equations

In this section, we derive linearised equations describing the small-amplitude free vibration about periodic steady state. In order to linearize the set of equations (Eqs. (1)-(5)), we introduce a perturbation relative to the steady state for every dependent variable as follows:

$$w(x,t) = w_{\mathrm{ss}}(x,t) + w_{\mathrm{tr}}(x,t), \tag{11}$$
$$z(t) = z_{\mathrm{ss}} + z_{\mathrm{tr}}(t), \tag{12}$$
$$F(t) = F_{\mathrm{ss}} + F_{\mathrm{tr}}(t), \tag{13}$$
$$I(t) = I_{\mathrm{ss}}(t) + I_{\mathrm{tr}}(t). \tag{14}$$

where the superscript "tr" stands for transient. By substituting the expressions into Eqs. (1)-(5), applying a multi-dimensional Taylor series expansion about the steady-state variables and retaining terms up to and including first order,

we find the following set of equations:

$$\rho A\frac{\partial^2 w_{\rm tr}}{\partial t^2}+EI\frac{\partial^4 w_{\rm tr}}{\partial x^4}+k_{\rm s}\sum_{n=-\infty}^{\infty}\delta(x-nL)w_{\rm tr} = F_{\rm tr}\delta(x-Vt), \tag{15}$$

$$M\frac{d^2 z_{\rm tr}}{dt^2}=-F_{\rm tr}, \tag{16}$$

$$F_{\rm tr}=f_1(t)I_{\rm tr}-f_2(t)\Delta_{\rm tr}, \tag{17}$$

$$\frac{dI_{\rm tr}}{dt}+f_3(t)I_{\rm tr}=f_4(t)(K_{\rm p}\Delta_{\rm tr}+K_{\rm d}\dot{\Delta}_{\rm tr}) -(f_5(t)\Delta_{\rm tr}-f_6\dot{\Delta}_{\rm tr}), \tag{18}$$

where $\Delta_{\rm tr}=z_{\rm tr}-w_{\rm c,tr}$ and

$$f_1(t)=\frac{2CI_{\rm ss}}{\Delta_{\rm ss}^2}=2\frac{Mg}{I_{\rm ss}}, \tag{19}$$

$$f_2(t)=\frac{2CI_{\rm ss}^2}{\Delta_{\rm ss}^3}=\sqrt{\frac{Mg}{C}}f_1(t), \tag{20}$$

$$f_3(t)=\frac{R\Delta_{\rm ss}^2-2C\dot{\Delta}_{\rm ss}}{2C\Delta_{\rm ss}}, \tag{21}$$

$$f_4(t)=\frac{\Delta_{\rm ss}}{2C}, \tag{22}$$

$$f_5(t)=\frac{I_{\rm ss}}{\Delta_{\rm ss}}\frac{\dot{\Delta}_{\rm ss}}{\Delta_{\rm ss}}=\sqrt{\frac{Mg}{C}}\frac{\dot{\Delta}_{\rm ss}}{\Delta_{\rm ss}}, \tag{23}$$

$$f_6=\frac{I_{\rm ss}}{\Delta_{\rm ss}}=\sqrt{\frac{Mg}{C}}. \tag{24}$$

Eqs. (15)-(18) form a set of three linear differential equations (1 PDE and 2 ODEs) and one algebraic equation, all having time-periodic coefficients, with four unknowns: $z_{\rm tr}$, $w_{\rm tr}$ (which includes $w_{\rm c,tr}$), $F_{\rm tr}$ and $I_{\rm tr}$; note that the equation of motion of the beam would also have a time-periodic coefficient if it was written in the reference system that moves with the load. Also note that we could have eliminated $F_{\rm tr}$ immediately by combining Eqs. (16) and (17), but we do so at a later stage.

Finally, we emphasize that $\omega_1=2\pi/T$ (defined in Eq. (8)) is the fundamental frequency of oscillation in the periodic coefficients of the equations.

5 Method of solution

In this section, we present the solution method used to find the stability boundary. In essence, we search for the existence of quasi-periodic/periodic solutions for the field variables in the plane of the control parameters $K_{\rm p}$ and $K_{\rm d}$. The case of oscillatory instability, on the one hand, and those of divergence and parametric resonance on the other are treated separately.

5.1 Oscillatory instability

In order to find the stability boundary, we formulate expressions for the variables based on Floquet's theorem as the product of periodic functions $P_z(t)=P_z(t+T)$, $P_w(t)=P_w(t+T)$, $P_F(t)=P_F(t+T)$ and $P_I(t)=P_I(t+T)$, respectively, and an exponential function:

$$z_{\rm tr}=P_z(t)e^{i\Omega t}, \tag{25}$$

$$w_{\rm c,tr}=P_w(t)e^{i\Omega t}, \tag{26}$$

$$F_{\rm tr}=P_F(t)e^{i\Omega t}, \tag{27}$$

$$I_{\rm tr}=P_I(t)e^{i\Omega t}, \tag{28}$$

with the constraint that the Floquet/characteristic multiplier $e^{i\Omega T}$ has magnitude 1 [50, 51]; this implies that the Floquet exponent $i\Omega$ is purely imaginary and the unknown Ω is real-valued.

The periodic functions are straightforwardly written as Fourier series:

$$P_z=\sum_{k=-\infty}^{\infty}Z_k e^{i\omega_k t}, \tag{29}$$

$$P_w=\sum_{m=-\infty}^{\infty}W_m e^{i\omega_m t}, \tag{30}$$

$$P_F=\sum_{k=-\infty}^{\infty}F_k e^{i\omega_k t}, \tag{31}$$

$$P_I=\sum_{k=-\infty}^{\infty}I_k e^{i\omega_k t}. \tag{32}$$

P_w is formulated with a different counter, but it is expressed in terms of the Fourier coefficients F_k of the interaction force below; ω_k and ω_m are defined as in Eq. (8). It is noted that the expressions in Eqs. (25)-(28) represent quasi-periodic functions since Ω is generally incommensurate with the frequencies ω_k and ω_m. As a result, the solution method described in this section is essentially a generalization of Hill's method [50] which employs strictly periodic functions with Ω known and commensurate with ω_k, like in the specific cases described below (Sect. 5.2).

To simplify the analysis, we reduce the number of unknowns as much as possible. To start with, we express P_w in terms of the Fourier coefficients F_k. When doing so, we should realize that the deflection at the contact point $w_{{\rm c,tr},k}$ (note the additional subscript k) induced by a moving (single) harmonic load $F_k e^{i\bar{\omega}_k t}$, where $\bar{\omega}_k=\Omega+\omega_k$, is composed of multiple harmonics spaced with the support-passing frequency (associated with the period $T=V/L$), as shown in

Appendix A:

$$w_{\mathrm{c,tr},k} = F_k \sum_{l=-\infty}^{\infty} h_{kl} \mathrm{e}^{\mathrm{i}(\bar{\omega}_k+\omega_l)t}, \quad \omega_l = l\frac{2\pi}{T}. \tag{33}$$

Summing over all the force components k, we obtain an expression for $w_{\mathrm{c,tr}}$ in terms of F_k:

$$w_{\mathrm{c,tr}} = \sum_{k=-\infty}^{\infty} F_k \sum_{l=-\infty}^{\infty} h_{kl} \mathrm{e}^{\mathrm{i}(\bar{\omega}_k+\omega_l)t}. \tag{34}$$

Introducing $m = k + l$ and $\omega_m = \omega_k + \omega_l$, we now obtain the following expression for $P_w(t)$:

$$\begin{aligned} P_w(t) &= \sum_{k=-\infty}^{\infty} F_k \sum_{l=-\infty}^{\infty} h_{kl} \mathrm{e}^{\mathrm{i}(\omega_k+\omega_l)t} \\ &= \sum_{m=-\infty}^{\infty} W_m \mathrm{e}^{\mathrm{i}\omega_m t}, \; W_m = \sum_{k+l=m} F_k h_{kl} \end{aligned} \tag{35}$$

Clearly, the lowest oscillation frequency ω_m is equal to $2\pi/T$ (for $k = 1$ and $l = 0$ or $k = 0$ and $= 1$), and thus P_w is periodic with period T, in correspondence with Floquet's theorem. We note that the equation of motion of the beam (Eq. (15)) is essentially solved now (the expression for $w_{\mathrm{c,tr}}$ is its solution evaluated at the contact point), which implies that we are left with a set of two ODEs and one algebraic equation to solve (i.e., Eqs. (16)-(18)).

To further reduce the number of unknowns, the Fourier coefficients F_k are written in terms Z_k. Substituting Eqs. (25) and (27) into Eq. (16), we easily find that

$$F_k = \bar{\omega}_k^2 M Z_k. \tag{36}$$

Now, the solutions (Eqs. (25)-(28)), written in condensed form and expressed in terms of Z_k where possible, read

$$z_{\mathrm{tr}} = \sum_{k=-\infty}^{\infty} Z_k \mathrm{e}^{\mathrm{i}\bar{\omega}_k t}, \tag{37}$$

$$w_{\mathrm{c,tr}} = \sum_{k=-\infty}^{\infty} \bar{\omega}_k^2 M Z_k \sum_{l=-\infty}^{\infty} h_{kl} \mathrm{e}^{\mathrm{i}(\bar{\omega}_k+\omega_l)t}, \tag{38}$$

$$F_{\mathrm{tr}} = \sum_{k=-\infty}^{\infty} \bar{\omega}_k^2 M Z_k \mathrm{e}^{\mathrm{i}\bar{\omega}_k t}, \tag{39}$$

$$I_{\mathrm{tr}} = \sum_{k=-\infty}^{\infty} I_k \mathrm{e}^{\mathrm{i}\bar{\omega}_k t}. \tag{40}$$

Clearly, the remaining unknowns are Z_k, I_k and Ω; the remaining equations to be solved are Eqs. (17) and (18).

The expressions shown in Eqs. (37)-(40) are now substituted into the remaining equations, resulting in

$$\begin{aligned} &\sum_{k=-\infty}^{\infty} \bar{\omega}_k^2 M Z_k \mathrm{e}^{\mathrm{i}\omega_k t} = f_1(t) \sum_{k=-\infty}^{\infty} I_k \mathrm{e}^{\mathrm{i}\omega_k t} \\ &- f_2(t) \sum_{k=-\infty}^{\infty} Z_k \left(\mathrm{e}^{\mathrm{i}\omega_k t} - \bar{\omega}_k^2 M \sum_{l=-\infty}^{\infty} h_{kl} \mathrm{e}^{\mathrm{i}\omega_{kl} t} \right), \end{aligned} \tag{41}$$

$$\begin{aligned} &\sum_{k=-\infty}^{\infty} \mathrm{i}\bar{\omega}_k I_k \mathrm{e}^{\mathrm{i}\omega_k t} + f_3(t) \sum_{k=-\infty}^{\infty} I_k \mathrm{e}^{\mathrm{i}\omega_k t} \\ &= \Big(f_4(t) K_{\mathrm{p}} - f_5(t) \Big) \\ &\quad \cdot \sum_{k=-\infty}^{\infty} Z_k \left(\mathrm{e}^{\mathrm{i}\omega_k t} - \bar{\omega}_k^2 M \sum_{l=-\infty}^{\infty} h_{kl} \mathrm{e}^{\mathrm{i}\omega_{kl} t} \right) \\ &\quad + \Big(f_4(t) K_{\mathrm{d}} + f_6 \Big) \\ &\quad \cdot \sum_{k=-\infty}^{\infty} Z_k \left(\mathrm{i}\bar{\omega}_k \mathrm{e}^{\mathrm{i}\omega_k t} - \bar{\omega}_k^2 M \sum_{l=-\infty}^{\infty} \mathrm{i}\bar{\omega}_{kl} h_{kl} \mathrm{e}^{\mathrm{i}\omega_{kl} t} \right), \end{aligned} \tag{42}$$

where $\bar{\omega}_{kl} = \bar{\omega}_k + \omega_l$ and $\omega_{kl} = \omega_k + \omega_l$. Note that the factor $\mathrm{e}^{\mathrm{i}\Omega t}$ has been dropped as it is common to all terms in the equations. Equations (41) and (42) form a system of two equations with one plus two sets of infinitely many unknowns.

The equations can be solved in an approximate manner by truncating the Fourier series (i.e., summations over k and l then run from $-N$ to N, where N is a finite number) and projecting both equations onto the complex conjugates of all harmonics involved in the periodic functions, that is, onto $\mathrm{e}^{-\mathrm{i}\omega_n t}$ with $n = \{-N, ..., N\}$. The resulting system of $4N+2$ equations reads

$$\begin{aligned} &\sum_{k=-N}^{N} \bar{\omega}_k^2 M \delta_{nk} Z_k \\ &= \sum_{k=-N}^{N} \Big(A_{1,nk} I_k - (A_{2,nk} - B_{2,nk}) Z_k \Big), \end{aligned} \tag{43}$$

$$\begin{aligned} &\sum_{k=-N}^{N} \Big(\mathrm{i}\bar{\omega}_k \delta_{nk} I_k + A_{3,nk} I_k \Big) = \sum_{k=-N}^{N} \Big(K_{\mathrm{p}} (A_{4,nk} \\ &- B_{4,nk}) Z_k - (A_{5,nk} - B_{5,nk}) Z_k + K_{\mathrm{d}} (\mathrm{i}\bar{\omega}_k A_{4,nk} \\ &- C_{4,nk}) Z_k + (\mathrm{i}\bar{\omega}_k A_{6,nk} - C_{6,nk}) Z_k \Big), \end{aligned} \tag{44}$$

where δ_{nk} represents the Kronecker delta. The system is rewritten in matrix–vector form:

$$\mathbf{A}_1 \mathbf{y} = (\mathbf{D} + \mathbf{A}_2 - \mathbf{B}_2)\mathbf{z}, \tag{45}$$

$$(\mathbf{E} + \mathbf{A}_3)\mathbf{y} = K_{\mathrm{p}}(\mathbf{A}_4 - \mathbf{B}_4)\mathbf{z} + \Big(K_{\mathrm{d}}(\mathbf{A}_4 \mathbf{E} - \mathbf{C}_4)$$

$$- (\mathbf{A}_5 - \mathbf{B}_5) + \mathbf{A}_6\mathbf{E} - \mathbf{C}_6\Big)\mathbf{z}. \tag{46}$$

Here, $\mathbf{y}$ and $\mathbf{z}$ are vectors containing I_k and Z_k, respectively, and the matrix entries are defined as follows, with $j = \{1, ..., 6\}$ (not all j are relevant for $A_{j,nk}$, $B_{j,nk}$ and $C_{j,nk}$):

$$A_{j,nk} = \frac{1}{T}\int_0^T f_j \mathrm{e}^{\mathrm{i}(\omega_k - \omega_n)t}\, dt, \tag{47}$$

$$B_{j,nk} = \frac{\bar{\omega}_k^2 M}{T}\int_0^T f_j \sum_{l=-N}^{N} h_{kl}\mathrm{e}^{\mathrm{i}(\omega_{kl} - \omega_n)t}\, dt, \tag{48}$$

$$C_{j,nk} = \frac{\bar{\omega}_k^2 M}{T}\int_0^T f_j \sum_{l=-N}^{N} \mathrm{i}\bar{\omega}_{kl} h_{kl}\mathrm{e}^{\mathrm{i}(\omega_{kl} - \omega_n)t}\, dt, \tag{49}$$

$$D_{nk} = \bar{\omega}_k^2 M \delta_{nk}, \tag{50}$$

$$E_{nk} = \mathrm{i}\bar{\omega}_k \delta_{nk}. \tag{51}$$

The matrix entries involving $f_6 \neq f_6(t)$ can be simplified; the relevant ones are

$$A_{6,nk} = f_6 \delta_{nk}, \tag{52}$$

$$\begin{aligned} C_{6,nk} &= \bar{\omega}_k^2 M f_6 \sum_{l=-N}^{N} \mathrm{i}\bar{\omega}_{kl} h_{kl} \delta_{n(k+l)} \\ &= \bar{\omega}_k^2 M f_6 \mathrm{i}\bar{\omega}_{k(n-k)} h_{k(n-k)}. \end{aligned} \tag{53}$$

Eqs. (45) and (46) are now combined to eliminate the vector $\mathbf{y}$. The resulting equation constitutes an eigenvalue problem:

$$\mathbf{G}\mathbf{z} = K_\mathrm{p}\mathbf{z}, \tag{54}$$

where

$$\begin{aligned} \mathbf{G} = {} & (\mathbf{A}_4 - \mathbf{B}_4)^{-1}(\mathbf{E} + \mathbf{A}_3)\mathbf{A}_1^{-1} \\ & \cdot \Big(\mathbf{D} + \mathbf{A}_2 - \mathbf{B}_2 - \mathbf{A}_1(\mathbf{E} + \mathbf{A}_3)^{-1}\mathbf{H}\Big), \end{aligned} \tag{55}$$

with

$$\mathbf{H} = K_\mathrm{d}(\mathbf{A}_4\mathbf{E} - \mathbf{C}_4) - (\mathbf{A}_5 - \mathbf{B}_5) + \mathbf{A}_6\mathbf{E} - \mathbf{C}_6. \tag{56}$$

To find the stability boundary in the plane of control gains K_p and K_d, the values of Ω (relevant for all matrices except the $\mathbf{A}_j$) and K_d (relevant for $\mathbf{H}$) are looped over, allowing to find the eigenvalues K_p numerically using a standard algorithm for each Ω, K_d pair. Whenever an obtained eigenvalue is real-valued, a quasi-periodic solution of the governing equations (Eqs. (15)-(18)) is found; hence, that specific K_p value is used to form the stability boundary together with other real-valued K_p values found for the same and other Ω, K_d pairs (see, for example, Fig. 2). Initial guesses for the latter variables, in the vicinity of which we search, are formulated based on the findings for the system with a fixed support, which are known analytically [15]. The value of Ω is limited to the principal value obtained from the Floquet multiplier $\mathrm{e}^{\mathrm{i}\Omega T}$, that is $0 \leq \Omega < \omega_1$, as oscillation frequencies outside this range are automatically incorporated due to the multiplication of $\mathrm{e}^{\mathrm{i}\Omega t}$ with the periodic functions (Eqs. (29)-(32)).

It is noted that the numerically computed eigenvalues are never strictly real-valued due to the fixed grid of Ω and K_d values applied in the search and due to small numerical inaccuracy. However, the imaginary part of the eigenvalues selected is typically several orders of magnitude smaller than those of the ones that are rejected, which makes the selection of the eigenvalues unambiguous. In addition, sensitivity studies of the obtained eigenvalues to the chosen grid (Ω and K_d) have been conducted for the results presented in Sect. 7, which ensures that these are accurate and complete (within the search range).

It is also noted that the method presented in the current section does not necessarily yield the actual stability boundary. A real-valued K_p found for a specific Ω, K_d pair indicates the existence of a bounded, non-decaying solution, but that does not guarantee stability. Other solutions that exist for the specific combination of Ω, K_d and K_p can in principle be unstable. A transient analysis employing a FEM-based numerical solution (simplified version of that presented in Ref. [52]) has therefore been used to check the actual behavior left and right of the obtained quasi-periodic solutions in the plane of control gains (see Sect. 7) to judge whether or not they are part of the stability boundary. It can be verified that the transient responses clearly decay and increase to the left and right of the actual boundary, respectively. The validation has been conducted for small speeds only, as the FEM code of Ref. [52] needs optimization to handle high speeds. We note, however, that the results for small speeds in fact validate the *methodology* presented in the current section.

In the general case of Ω being non-zero and not equal to $\frac{1}{2}\omega_1$, the stability boundary marks the emergence of an oscillatory or flutter-type instability [50, 51]. The mentioned specific cases are related to divergence and parametric resonance, as discussed next.

5.2 Divergence and parametric resonance

Motivated by findings for the continuously supported beam and rigid-base systems where part of the stability boundary relates to a divergence instability [15, 37], we consider the specific case of $\Omega = 0$ and only the constant parts of the periodic functions included in the solution. In that case, the governing equations (Eqs. (15)-(18)) can be solved exactly.

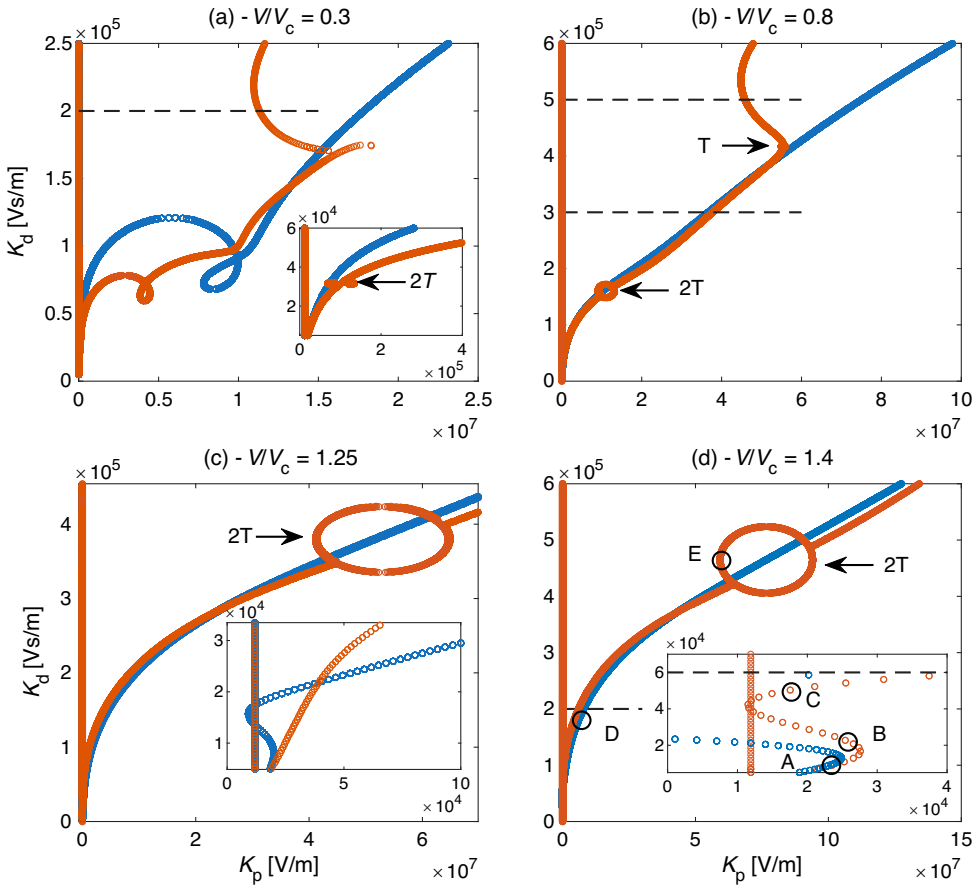

Fig. 2 Stability boundaries of the weakly periodic (red) and non-periodic (blue) systems, for increasing relative speed V/V_c

Assuming

$$\begin{aligned} z_{tr} &= Z_0, \\ w_{c,tr} &= W_0, \\ F_{tr} &= F_0, \\ I_{tr} &= I_0, \end{aligned} \tag{57}$$

where other components F_k (with $k \neq 0$) that do contribute to W_0 are excluded as these would render $w_{c,tr}$ and z_{tr} non-constant, we find based on Eq. (36) that $F_0 = \omega_0^2 M Z_0 = 0$ because $\omega_0 = 0$. Thus, $W_0 = F_0 h_{00} = 0$ too (see Eq. (35)), which implies that the beam is not loaded at all. Equation (17) then yields (using Eq. (9))

$$Z_0 = \frac{\Delta_{ss}}{I_{ss}} I_0 = \sqrt{\frac{C}{Mg}} I_0. \tag{58}$$

Substituting this expression into Eq. (18) and using Eq. (21) leads to

$$\left(K_p - R \frac{I_{ss}}{\Delta_{ss}} \right) I_0 = 0, \tag{59}$$

from which the following expression is obtained (as $I_0 \neq 0$):

$$K_p = R \frac{I_{ss}}{\Delta_{ss}} = R \sqrt{\frac{Mg}{C}}. \tag{60}$$

Eq. (9) was used for the last step. Clearly, the part of the stability boundary described by Eq. (60) is fully governed by the electromagnetic system, the flexible beam has no influence at all (which is to be expected as $W_0 = 0$). The result is the same as that of the system with rigid support as well as that of the system having a flexible beam with distributed, constant support stiffness [15, 37]. As stated, for these systems the instability observed by crossing the boundary (to the region $K_p < R\sqrt{Mg/C}$) is a divergence instability. It was demonstrated that the controller becomes to weak then, so that small perturbations relative to the steady state lead to mass falling down/collide with the beam [37]. The same divergence instability being observed for the current system is related to the steady-state position of the mass being constant, which leads to the time-periodicity of the system (i.e., of the coefficients in the governing equations) dropping when the solution composed of constants (Eq. (57)) is substituted (as shown in Eqs. (58) and (59)).

For the specific case of T parametric resonance, Ω is known a priori and can be equated to 0 [50], as the fact of the

response being periodic with period T is already accounted for by the periodic functions (Eqs. (25)-(28)). In this case, the solution method presented in the previous section essentially reduces to Hill's method. The part of the stability boundary related to T parametric resonance can be found by solving the eigenvalue problem (Eq. (54)), but we only need to loop over K_d in this particular situation. Furthermore, as the specific case of $\Omega = 0$ with only the constant parts of the periodic functions included in the solution can be considered separately (see previous paragraph) and leads to another part of the boundary which is unrelated to parametric resonance, the terms associated with the constants of the periodic functions (i.e., Z_0 and I_0, and thus F_0 as well as the part of W_0 related to F_0) can be left out from the Eqs. (41) and (42) in composing the eigenvalue problem (Eq. (54)) for T parametric resonance; in fact, the two sets of equations turn out to be completely decoupled.

For the specific case of $2T$ parametric resonance, Ω is also known a priori and can be equated to $\frac{1}{2}\omega_1 = \pi/T$ [41, 50], which leads to a periodic solution with period $2T$ (see Eqs. (25)-(28)). In this case, the solution method is again Hill's method, and the part of the stability boundary related to $2T$ parametric resonance can be found by solving the eigenvalue problem (Eq. (54)) by looping over K_d. Note that the constant parts of the periodic functions do have to be included in this case; when combined with the exponential function $\mathrm{e}^{\mathrm{i}\Omega t}$, they capture the fundamental oscillation with period $2T$.

6 Energy analysis

The method presented in Sect. 5 is rather straightforward and (when combined with a transient analysis) yields the stability boundary, but it fails to differentiate between the two instability mechanisms, that is, between the wave-induced and electromagnetic instability mechanisms related to the guideway's reaction force and the electromagnetic force, respectively (see Sect. 1). Consequently, defining effective mitigation strategies to stabilize the system remains impossible. To identify the energy input by the two forces separately, we here present an expression for the energy balance of the moving mass, similar to that of Fărăgău et al. [37]. The linearized equations of motion are used.

The variation of the kinetic energy ($E_\mathrm{M} = \frac{1}{2}M\dot{z}_\mathrm{tr}^2$) of the moving mass can be obtained by multiplying both sides of the equation of motion of the discrete mass (Eq. (16)) by its velocity $\dot{z}_\mathrm{tr}$. Through manipulation of the left-hand side, the following expression is obtained:

$$\frac{d}{dt}E_\mathrm{M} = -F_\mathrm{tr}\frac{dz_\mathrm{tr}}{dt}. \tag{61}$$

Adding and subtracting the term $F_\mathrm{tr}\dot{w}_\mathrm{c,tr}$ on the right-hand side, the energy variation law can be written as follows:

$$\frac{d}{dt}E_\mathrm{M} = -F_\mathrm{tr}\frac{d\Delta_\mathrm{tr}}{dt} - F_\mathrm{tr}\frac{dw_\mathrm{c,tr}}{dt} = P_\mathrm{em} + P_\mathrm{gw}. \tag{62}$$

Integration Eq. (62) over the time interval $[t_0, t_1]$ yields the energy balance:

$$\begin{aligned} E_\mathrm{M}(t_1) - E_\mathrm{M}(t_0) &= \int_{t_0}^{t_1} P_\mathrm{em}\,dt + \int_{t_0}^{t_1} P_\mathrm{gw}\,dt \\ &= W_\mathrm{em} + W_\mathrm{gw}. \end{aligned} \tag{63}$$

Eq. (63) shows that there are two main contributions to the (kinetic) energy variation $E_\mathrm{M}(t_1) - E_\mathrm{M}(t_0)$ of the mass: (i) the energy input/work done by the electromagnetic force (W_em) and (ii) the energy input/work done by the guideway's reaction force (W_gw), respectively. Positive input represents energy added to the mass vibration, while negative input represents energy dissipation. Since both forces can be stabilizing or destabilizing, they either extract energy from or input energy into the vehicle vibration. Note that, since the responses are generally quasi-periodic, the oscillation period (to integrate over) is not well defined. Therefore, in the numerical analyses (Sect. 7), t_0 is chosen equal 0 and the energy inputs are plotted for running t_1 to reveal the trends. Furthermore, we note that the two contributions to the energy balance (on average) cancel at the stability boundary. For $W_\mathrm{gw} > 0$, the guideway's reaction force inputs energy into the mass-suspension system, which is then dissipated by the electromagnetic force: $W_\mathrm{em} < 0$. For $W_\mathrm{em} > 0$, the electromagnetic force inputs energy into the mass vibration, which is then dissipated by the beam through radiation damping (and some viscous damping if considered): $W_\mathrm{gw} < 0$. Finally, we note that the (positive) energy input by guideway's reaction force essentially originates from the (horizontal) force needed to maintain the movement of the mass at constant speed V [37, 53].

The energy analysis requires real-valued response quantities as input to be meaningful. However, the solution used for determining the stability boundary (Eqs. (25)-(28)) is generally complex-valued. To overcome this, another solution is determined with the exponential function being the complex conjugate of the original one (i.e., with $\mathrm{e}^{-\mathrm{i}\Omega t}$), and it is added to the original solution. As not all Fourier coefficients contained in the vectors $\mathbf{y}$ and $\mathbf{z}$ can be determined from the eigenvalue problem in Eq. (54) (and subsequently applying Eq. (45) or Eq. (46)) – note that only the eigenvector is known – unit values are chosen for the first entry of $\mathbf{z}$ for both solutions.

7 Results and Discussion

In this section, we present the obtained numerical results graphically, formulate relevant observations and relate those to the wave dynamics in the beam-foundation system. We consider two cases, one weakly inhomogeneous (periodic) system and one strongly inhomogeneous (periodic) system. The difference lies in the value of the non-dimensional parameter $k_s L^3/EI$ (equals 73.4 for the former, 367 for the latter) that characterizes the inhomogeneity of the beam-foundation system [54]. All parameter values have been taken/derived from Ref. [37]: $EI = 25 \cdot 10^6$ kNm^2, $\rho A = 1400$ kg/m, $M = 7650$ kg, $C = 0.05$ Nm^2/A^2, $L = 16$ m, $k_s = 44.8 \cdot 10^4$ kN/m^2 and $\Delta_{ss} = 15$ mm. They are the same for both cases, except the bending stiffness (five times smaller in the second case). Results for the periodic systems are compared to those of the equivalent non-periodic system having a continuously supported beam with constant support stiffness. The distributed-support stiffness k_d of the latter system is obtained by smearing the discrete-spring stiffness: $k_d = k_s/L$. Results for the non-periodic system have been obtained using the method presented in Ref. [37]. For ease of comparison, the critical speed (for resonance) V_c used to formulate the relative speed (V/V_c) of the mass is defined based on the non-periodic system (without damping; i.e., the minimum phase velocity). It is also used when presenting results for the periodic system, although it is not an actual critical speed of the latter.

For practical relevance, viscous damping has been added to the supports and the beam by introducing complex stiffnesses: $k_s \rightarrow k_s + \mathrm{i}\omega c_s = k_s(1+\mathrm{i}\omega\zeta)$ and $E \rightarrow E(1+\mathrm{i}\omega\zeta)$. Here, c_s is the viscous-damping coefficient of the discrete supports, and ζ denotes the (viscous) damping ratio; for simplicity the damping ratios of the supports and the beam have been assumed identical. The support-damping value has been derived from Ref. [37] by lumping: $c_s = c_d L$, where c_d is the viscous-damping coefficient of the distributed support. The obtained $\zeta = 7 \cdot 10^{-4}$, which is clearly not small.

For the numerical results presented below, $N = 5$ has been chosen in the truncation of the Fourier series (Sect. 5). It can be verified that this leads to converged results. More specifically, the relative error in the eigenvalues (K_p locations) compared to those obtained using $N = 10$ is in the order of 10^{-5} (at most) for all analyses.

7.1 Weakly inhomogeneous system

Stability boundary

Figure 2 presents the lines along which quasi-periodic solutions are found in the plane of the control parameters K_p and K_d, for both the periodic and non-periodic systems and for increasing relative speed V/V_c. Note that all K_p, K_d pairs associated with real-valued eigenvalues are depicted, while not all of them are part of the actual stability boundary, as discussed in Sect. 5. The transient analysis allowed identifying the stable and unstable zones; the zone between the left straight line and the leftmost part of the curved line on the right (that contains loops and/or ellipses) is the stable zone. Obviously, the interface between the stable and unstable zones is the actual stability boundary.

Figure 2 clearly shows similarities and differences between the results for the periodic and non-periodic systems. First of all, both systems share the same left boundary; it is related to the divergence instability discussed in Subsection 5.2, and it is found at the K_p value shown in Eq. (60). Furthermore, the overall shape of the stable zone for both systems is roughly triangular, like for the 1.5 DOF system analysed by Paul et al. [15] (i.e., system with rigid base). For small relative velocity ($V/V_c = 0.3$), the line of quasi-periodic solutions on the right has a small loop at small K_p, K_d for both systems, although the exact locations differ. For large V/V_c, the right boundary 'bends back' (i.e., has an S-shape) locally at small K_p, K_d for both systems cutting the stable zone in two parts, although the speed at which this happens differs: appr. $V/V_c = 1.25$ for the non-periodic system and appr. $V/V_c = 1.4$ for the periodic system.

One of the important differences between the periodic and non-periodic systems is the occurrence of elliptical indentations of the right Stability boundary of the former, related to T and $2T$ parametric resonances. For small relative speed, the elliptical indentations are very small in size, but for large speed their sizes become larger, although the relative sizes (compared to the local width of the stable zone) seem hardly affected. They also shift upward, which is reasonable as the basic frequency of parametric excitation (ω_1) increases with increasing speed and, for parametric resonance to occur, it needs to match a frequency of free oscillation of the system, which typically increases along the right boundary [15, 37]. In addition to the parametric resonance zones, there is significant amorphous indentation for the periodic system; see $V/V_c = 0.3$ and $V/V_c = 0.8$ (Fig. 2). This indentation moves upward with increasing speed; for $V/V_c = 0.8$, it is only partially present in the chosen K_p, K_d window.

For very large vehicle speed (not shown), the inertia and bending effects will dominate the response of the beam, and hence the specific nature of the foundation will no longer be influential. Therefore, all indentations (also the ones related to parametric resonance) will be very minor and the stability boundaries of the periodic and non-periodic systems will be very similar.

Regarding the type of the instability, we note that the parts of the right stability boundary unrelated to parametric resonances mark the emergence of an oscillatory/flutter-type instability, as Ω is non-zero and not equal to $\frac{1}{2}\omega_1$ (see also Sect. 5). This is also true for the amorphous indentation.

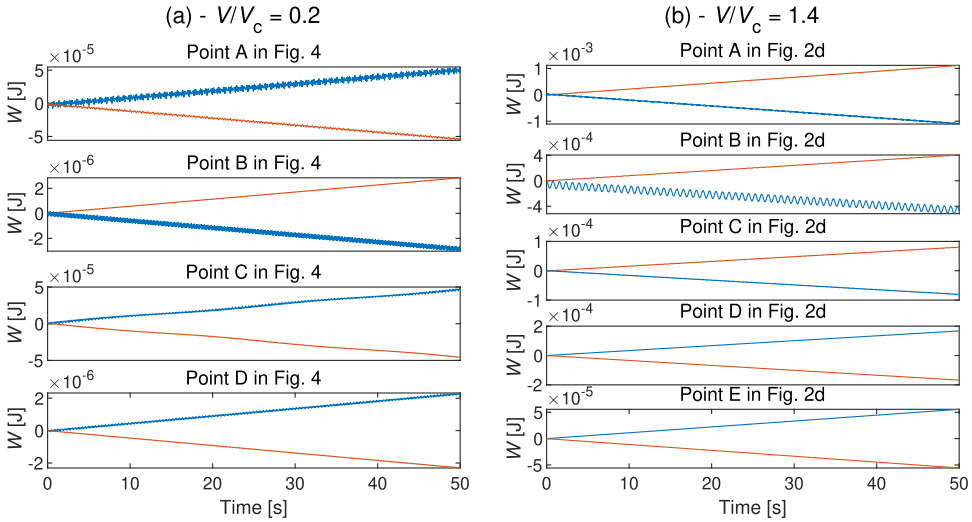

Fig. 3 Energy inputs W_{em} (blue) and W_{gw} (orange) for $V/V_c = 0.2$ (panel a) and $V/V_c = 1.4$ (panel b), for the weakly inhomogeneous system

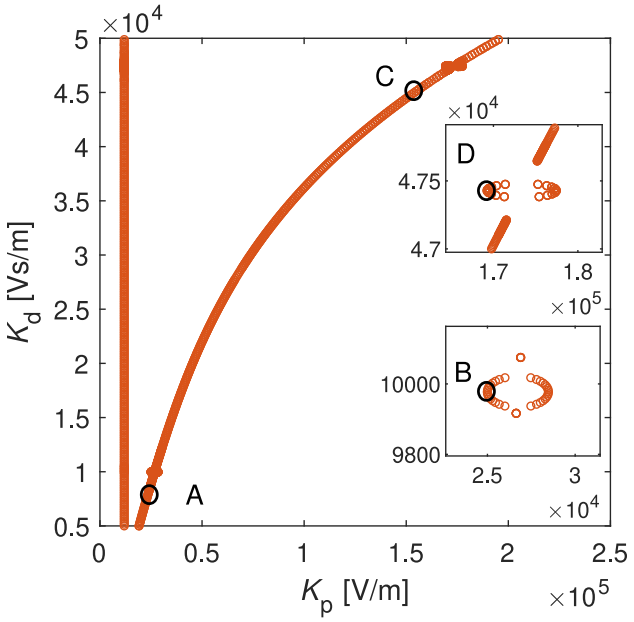

Fig. 4 Stability boundary of the weakly inhomogeneous system for $V/V_c = 0.2$

Energy analysis

The energy inputs shown in Fig. 3 (corresponding stability boundary is shown in Figs. 2 and 4) for points along the right stability boundary reveal that it is mostly the electromagnetic force that destabilizes the periodic system for small relative speeds, like for the non-periodic system [37]. This can be inferred from the fact that the energy input by the electromagnetic force (W_{em}) is positive and the energy input by the guideway's reaction force (W_{gw}) is negative (see Sect. 6). The contributions balance each other at the stability boundary, but just to the right of it the force with positive energy input will cause instability; for simplicity, we therefore write that the instability is electromagnetics induced (or wave induced in the opposite case). We encountered one exception, at small relative speed $V/V_c = 0.2$; see Fig. 4. As shown in Fig. 3, the $2T$ parametric resonance for this speed is wave induced, but along the rest of the boundary, including the T parametric resonance, the instability is electromagnetics induced. For other small relative speeds investigated (e.g., Fig. 2), the $2T$ parametric resonance is electromagnetics induced too. Clearly, the anomalous Doppler waves which feedback energy into the vehicle vibration (see Sect. 1) – in contrast to the non-periodic system, a moving load does excite waves (incl. anomalous Doppler waves) even at small relative speeds in the periodic system (see wave analysis below) – are not that strong, meaning that the guideway reaction force is usually dominated by the regular Doppler waves which extract energy from the vehicle vibration (i.e., provide radiation damping).

At large relative speed, for example at $V/V_c = 1.4$ (see Fig. 3), the energy inputs provide a picture for the periodic system that is again generally similar to that of the non-periodic system. There is a clear distinction between regions of wave-induced (small K_p, K_d) and electromagnetic (large K_p, K_d) instability [37]. Furthermore, it turns out that the bending back of the stability boundary addressed above is due to the wave-induced instability mechanism; the energy input by the guideway's reaction force is apparently so strong that the electromagnetic force cannot dissipate the energy for many K_p, K_d combinations, which leads to a significant reduction of the size of the stable domain (compared to the original size for very small V), like for the non-periodic system [37]. The $2T$ parametric resonance is in this case electromagnetics induced; this is the case for all other scenarios analyzed as well (including T parametric resonance), even for the strongly inhomogeneous system treated in Subsection 7.2.

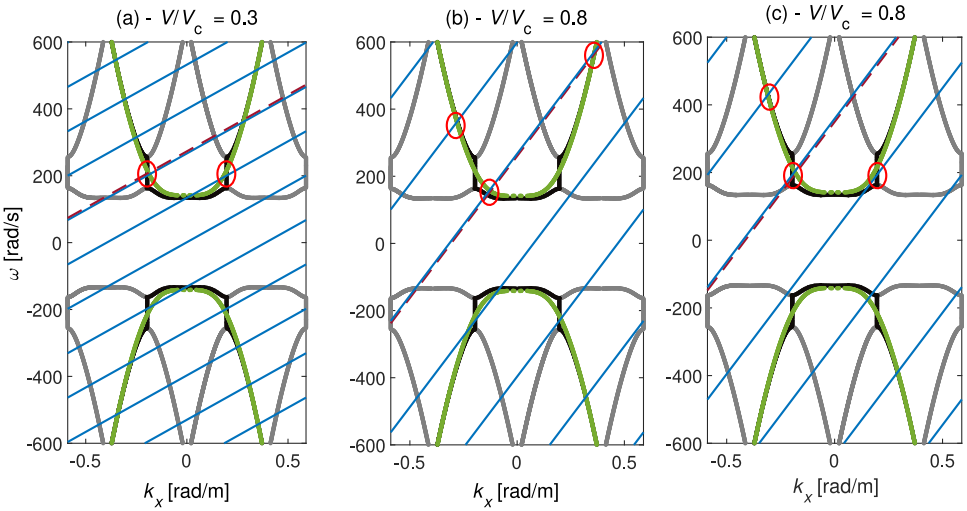

Fig. 5 Dispersion curve (grey, black) and kinematic invariants (blue) for $V/V_c = 0.3$ (panel a) and $V/V_c = 0.8$ with the medium (panel b) and large (panel c) K_d values indicated in Fig. 2. The solid black line indicates the primary dispersion curve, and the green line indicates that of the non-periodic system. Red circles indicate intersections between the primary dispersion curve and kinematic invariants. The dashed red line is the kinematic invariant of the non-periodic system

Wave analysis

We now relate the similarities and differences regarding the shape of the right stability boundary (Fig. 2) to the specific waves excited by the moving mass to provide some fundamental understanding. Figure 5 shows the dispersion curves of the periodic [55–57] and non-periodic systems; both curves relate to the undamped system to ensure a clear distinction between propagating and evanescent waves, but it should be noted that the actual systems are lightly damped (see first paragraph of Sect. 7). Apart from the stop band between appr. 150 and 250 Hz for the periodic system (and the multiple Brillouin zones), the differences between the curves are not that big; note, for example, that the cut-off frequencies are very similar. This is reasonable as the periodic system is only weakly inhomogeneous. The kinematic invariants expressing the frequency-wavenumber content of the moving oscillatory contact force (see Appendix A, with the replacements specified at the end), defined as

$$\omega = \bar{\omega}_k + \omega_l + k_x V = \Omega + \omega_m + k_x V, \tag{64}$$

with m being an integer and $\omega_m = \omega_k + \omega_l$ (see Sect. 5), are shown in Fig. 5 too, for different V/V_c and the K_d values indicated in Fig. 2 (K_d determines Ω; see Sect. 5). Note that there are infinitely many kinematic invariants (with spacing ω_1) for the periodic system, while there is only one for the non-periodic system; the kinematic invariant of the latter can be found by leaving out ω_m, but one should realize that the fundamental frequency of oscillation Ω is in principle different for the periodic and non-periodic systems. Intersections (indicated by red circles) of the kinematic invariants with the dispersion curve generally indicate the frequencies (ω) and wavenumbers (k_x) of the waves that are excited. For the current wave analysis, considering intersections with the black line, which is the primary dispersion curve, are sufficient for determining the excited wave types; note that the primary dispersion curve is composed of adjacent branches from neighboring Brillouin zones [58] that will reduce to the smooth dispersion curve of the non-periodic system when the inhomogeneity becomes very small.

For the specific, medium K_d value indicated in Fig. 2(b), the values of Ω are very similar for the periodic and non-periodic systems, and propagating waves are excited having nearly the same frequency as the dispersion curves are very similar at the (most important) intersection with the kinematic invariants; see Fig. 5(b) (it can be verified that the wave with lowest ω (middle circle) dominates the behaviour of the periodic system in this specific situation). This explains the similarity of the shape of the right stability boundary in Fig. 2(b) for $V/V_c = 0.8$ and the medium K_d value. However, for the relatively large K_d value chosen at the level of the amorphous indentation (Fig. 2(b)), the types of excited waves are different, as shown in Fig. 5(c); the first higher-order ($m = 1$) kinematic invariant crosses (middle circle) the dispersion curve in a stop band (the fundamental one, $m = 0$, too: right circle), which implies that one of the excited waves in the periodic system is evanescent. The dynamic behaviour is therefore very different from that of the non-periodic system. An evanescent wave does not provide radiation damping as it does not carry energy away from the source, which results in the much more narrow stable domain (Fig. 2(b)), even though the system is only weakly inhomogeneous.

The upward shift of the amorphous indentation with increasing speed addressed above can be understood by comparing panels (a) and (c) of Fig. 5. For the smaller speed $V/V_c = 0.3$ (Fig. 5(a)), for which the kinematic invariants have a relatively small slope, the $m = 2$ invariant crosses (left circle) the stop band (the $m = 1$ invariant too: right circle). For the increased speed $V/V_c = 0.8$, the $m = 1$ invariant crosses (middle circle) the stop band (the $m = 0$ invariant too: right circle) due to the larger slope and the larger spacing between the invariants. However, for this kinematic invari-

ant to cross the stop band, the value of Ω must increase too from $V/V_c = 0.3$ to 0.8. The larger Ω typically comes with a larger K_d value [15], and as a consequence, the amorphous indentation must shift upward as the velocity increases.

Interestingly, parametric resonance is observed for $V/V_c = 0.8$ when one ore more of the kinematic invariants cross the dispersion curve at the edge of a pass band. Figure 6 shows that T parametric resonance takes place when the $m = 1$ kinematic invariant crosses (left circle) the dispersion curve at the upper edge of the first pass band (the $m = 0$ invariant crosses too: right circle), while for $2T$ parametric resonance, the $m = 0$ invariant crosses the dispersion curve at/very close to the lower edge of the first pass band (i.e., at the cut-off frequency). At the edge of a stop band, the wave is a truly standing wave. When the beam dynamics is dominated by a standing wave, the beam just oscillates according to the standing wave mode and no or hardly any energy propagates, creating a situation which is in some ways similar to that of a discrete system with oscillating base, where parametric resonance also takes place [15]. However, the relation between parametric resonance and the occurrence of a standing wave is certainly not general. Considering T parametric resonance for slightly higher velocity, for example, the slope of the kinematic invariants will increase while they do not translate vertically (note that $\Omega = 0$). The crossings with the primary dispersion curve indicated in Fig. 6(a) will then shift into the stop band and additional crossings will emerge in the first pass band, implying that both evanescent and propagating waves are excited in that case but no standing wave. Furthermore, it should be noted that, in the exceptional case that parametric resonance is wave induced (as observed for the $2T$ resonance when $V/V_c = 0.2$; see Figs. 3(a) and 4), there must be an anomalous Doppler wave (defined below) that is sufficiently energetic to render the guideway's reaction force destabilizing. A dedicated in-depth energy analysis (preferably for a beam without damping) would be required to confirm this and could generally provide more clarity regarding the relation between parametric resonance and the occurring (energetic) wave types, but that is beyond the scope of the current paper.

Regarding the anomalous Doppler waves, it is impossible to predict that the instability is wave induced by solely checking the occurrence of such waves. As said, the waves exist in the periodic system for any non-zero V; by definition, the negative-frequency waves (i.e., indicated by crossings of the kinematic invariants and the dispersion curve) are anomalous Doppler [37, 53], and such crossings clearly exist always. For the non-periodic system, as soon as the anomalous Doppler waves are excited, they typically dominate the guideway's reaction force [37]. This is not the case for the periodic system. Figure 7 shows the ω, k_x graphs with Ω based on K_d values related to both wave-induced and electromagnetic instabilities (for $V/V_c = 1.4$; see Fig. 2(d)). In both situations anomalous Doppler waves are excited, and the number of anomalous Doppler waves in the considered frequency range is even the same: two crossings in each of the cases. The above-mentioned in-depth energy analysis could reveal which of the wave types (anomalous vs. normal Doppler) is most energetic and dictates the guideway's reaction force with varying K_d and even with varying V.

7.2 Strongly inhomogeneous system

Stability boundary

We here discuss the results for the strongly inhomogeneous system following the same structure as for the weakly inhomogeneous system. Figure 8 presents the stability boundaries in the K_p, K_d plane, for both the strongly inhomogeneous and non-periodic systems and for increasing relative speed. Clearly, the lines along which quasi-periodic solutions exist have multiple loops for small relative speeds (as discussed, these are not part of the actual stability boundary). In contrast to the weakly inhomogeneous system, the $2T$ parametric-resonance indentation is now very large relative to the width of the stable zone, even for smaller speeds (e.g., $V/V_c = 0.8$). This is in line with observations for the classical Mathieu equation [50], where the size of the unstable tongues increases with increasing magnitude of the parametric excitation. The bending back of the right stability boundary for small K_d (cf. Figure 2) is still observed for the current system (at $V/V_c = 1.4$). Furthermore, the stable zone can be significantly more narrow than that of the non-periodic system at small relative velocity (e.g., $V/V_c = 0.8$). Finally, the amorphous indentation still exists, although it may interfere with the parametric-resonance indentations, as is clear for V/V_c being 0.8, 1.25 and 1.4.

Energy analysis

As for the energy inputs, the picture is qualitatively the same as for the weakly inhomogeneous case. For small relative velocity, for example $V/V_c = 0.3$ (Fig. 9(a)), the instability at the right boundary is electromagnetics induced; we did not encounter any exceptions like for the weakly inhomogeneous case (cf. Figures 3(a) and 4), but we cannot exclude those either. In any case, the instability is mostly electromagnetics induced. For large relative velocity, for example $V/V_c = 1.25$ (Fig. 9(b)), the instability is wave induced for lower K_d values, while it is electromagnetics induced for larger K_d values, like for the weakly inhomogeneous system; see cf. Figure 3(b). Finally, we note that all parametric resonances encountered (also at speeds other than shown in Fig. 9) are electromagnetics induced.

Wave analysis

The dispersion curve (see Fig. 10) confirms that the system is strongly inhomogeneous. This manifests itself in the lowest branch displaying anomalous dispersion (not be confused

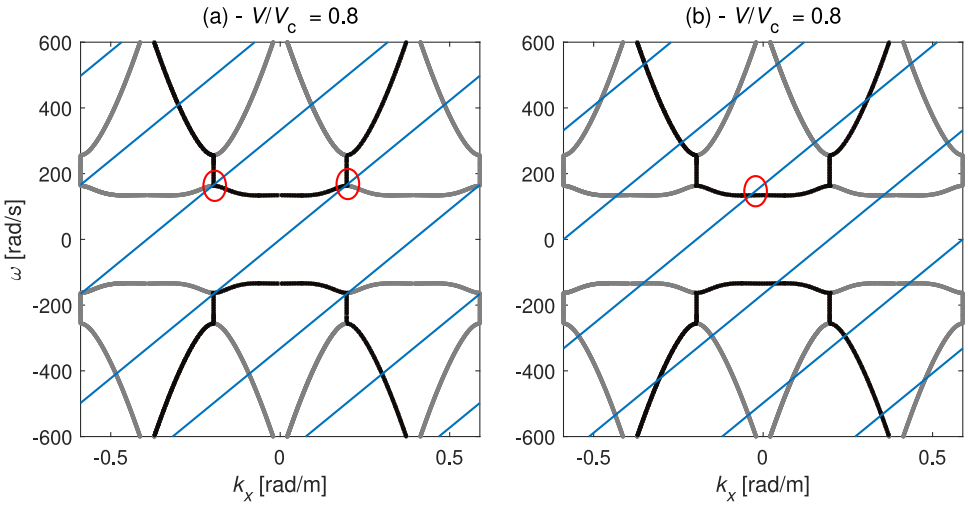

Fig. 6 Dispersion curve (grey, black) and kinematic invariants (blue) for $V/V_c = 0.8$ and K_d values corresponding with T (panel a) and $2T$ (panel b) parametric resonances (see Fig. 2(b)). The solid black line indicates the primary dispersion curve. Red circles indicate intersections between the primary dispersion curve and kinematic invariants

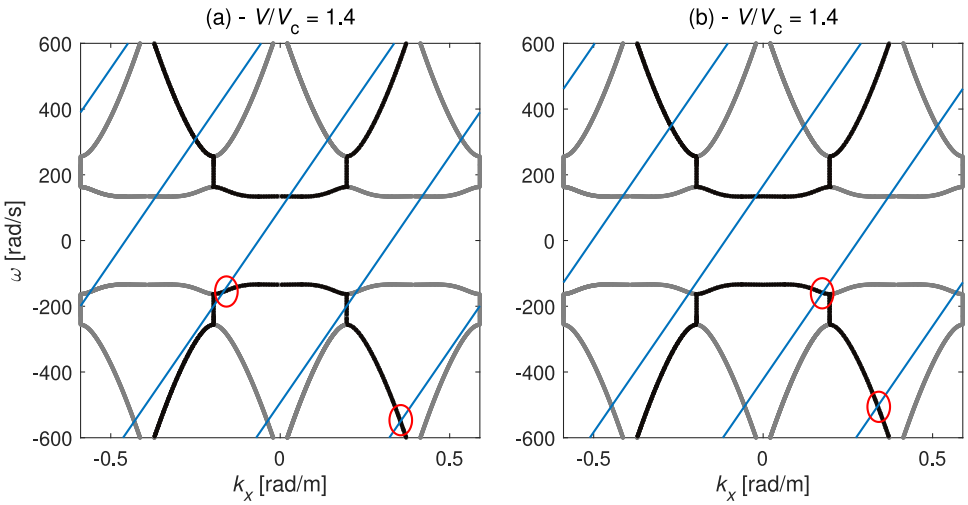

Fig. 7 Dispersion curve (grey, black) and kinematic invariants (blue) for $V/V_c = 1.4$ and the small (panel a) and medium (panel b) K_d values indicated in Fig. 2(d). The solid black line indicates the primary dispersion curve. Red circles indicate intersections between the primary dispersion curve and kinematic invariants

with anomalous Doppler waves), which is typical for strongly inhomogeneous systems. Clearly, the dispersion curve of the periodic system is very different from that of the non-periodic system.

As for the amorphous indentation, we can verify that it again happens when a kinematic invariant crosses a stop band, like for the weakly inhomogeneous system; as shown in Fig. 10(a)), the dispersion curve is even crossed in two stop bands for $V/V_c = 0.3$.

Figure 10 confirms that parametric resonance is not generally related to a standing wave in the beam. Although the $m = 0$ kinematic invariant crosses the dispersion curve at the upper edge of the first pass band for $2T$ parametric resonance (Fig. 10(c)) at the specific speed of $V/V_c = 0.8$, this will generally not be the case for other speeds (see reasoning in Subsection 7.1); also, no kinematic invariant crosses the dispersion curve at the edge of a pass band when T parametric resonance takes place (Fig. 10(b)) for the current speed.

7.3 Influence of damping

As mentioned in the introductory part of Sect. 7, the systems considered contain viscous damping. A comprehensive study into the effect of the damping on the stability boundary is beyond the purpose of the paper, but to get a preliminary idea, the viscous-damping ratio (ζ) has been varied by a factor 2 (smaller and larger), for both the weakly and the strongly inhomogeneous systems and for two values of the relative speed (small and large). Results are shown in Figs. 11 and 12. It can be observed that the left boundary is not affected, which makes sense as the divergence instability is fully governed by the electromagnetic system (Sect. 5.2). The right boundary shifts to a more or lesser extent, and the influence of a change in damping is generally more pronounced for larger K_p and K_d values. This is reasonable as the frequency of free oscillation of the system increases along the right boundary [15, 37], which enlarges the influence of the viscous forces. Note that increasing the damping does not necessarily imply that the stable zone increases in size; the

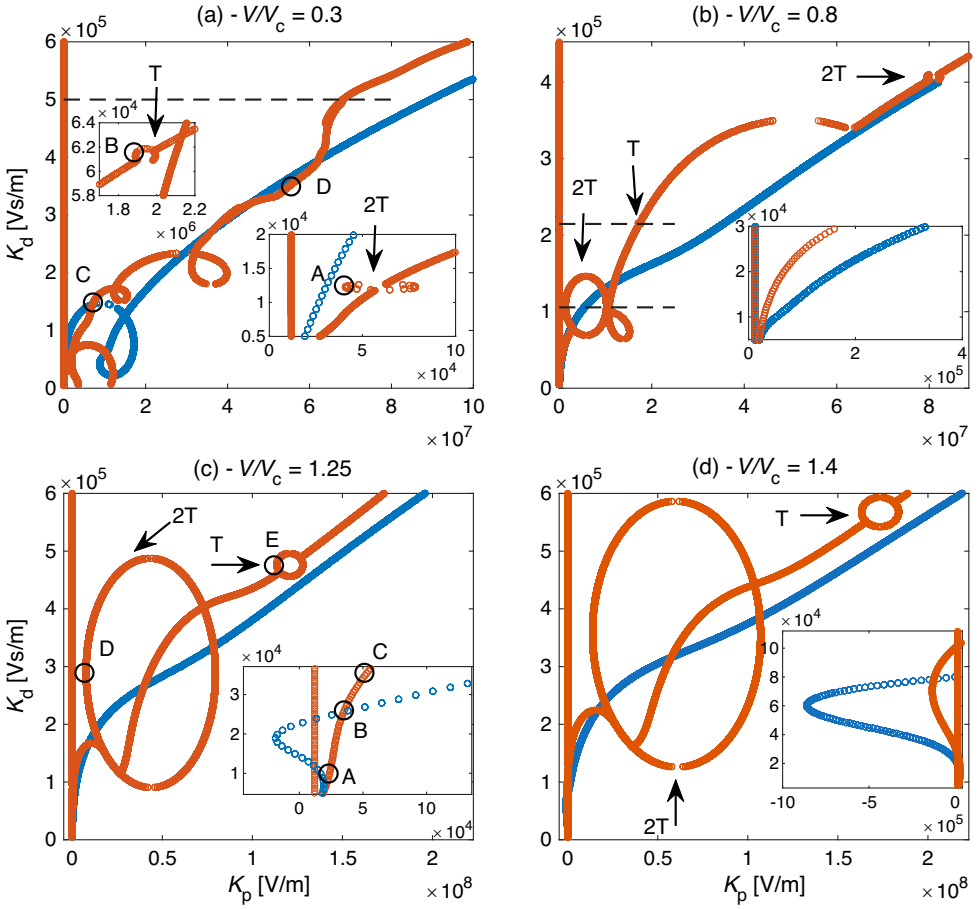

Fig. 8 Stability boundaries of the strongly periodic (red) and non-periodic (blue) systems, for increasing relative speed V/V_c

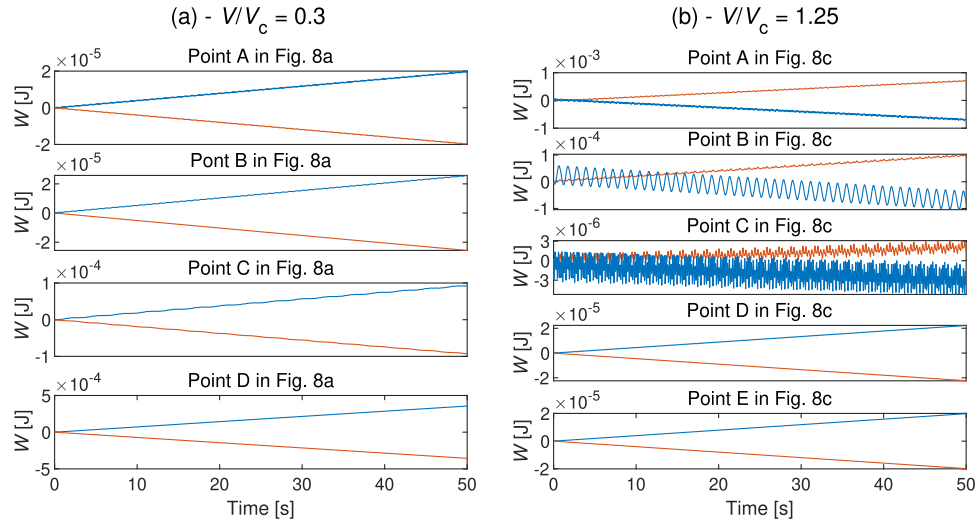

Fig. 9 Energy inputs W_{em} (blue) and W_{gw} (orange) for $V/V_c = 0.3$ (panel a) and $V/V_c = 1.25$ (panel b), for the strongly inhomogeneous system

reason is that a change in damping also affects the dynamic stiffness of the system, which leads to an overall change in the energy balance. The amorphous indentation and the loops (which are not part of the actual stability boundary) are significantly affected by the changes in damping. The parametric resonance ellipses mostly shift slightly (i.e., move along with the rest of the boundary), but hardly change in size. Finally, in the area where wave-induced instability takes place (small K_p, K_d range in Figs. 11(b) and 12(b)), the strength of the bending back of the stability boundary is rather seriously affected. The viscosity does clearly influence the strength of the energy feedback associated with the anomalous Doppler waves, which makes complete sense. Altogether, the find-

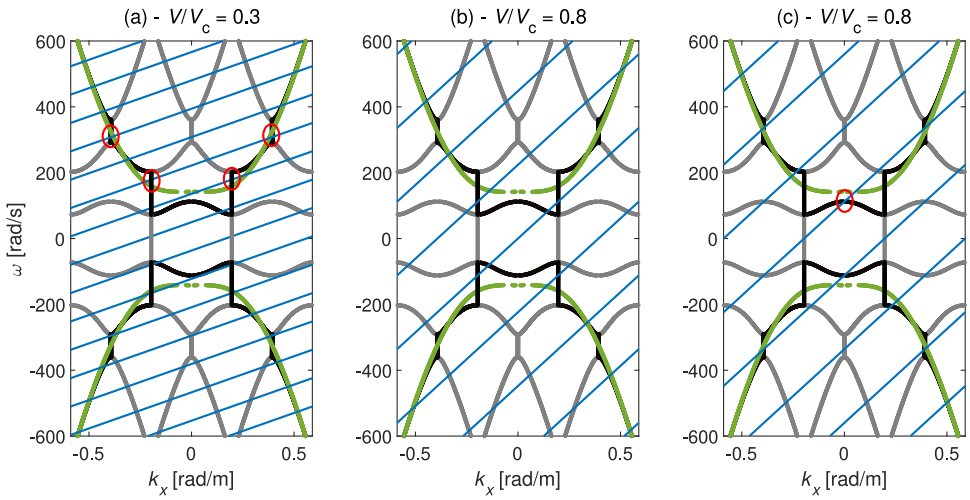

Fig. 10 Dispersion curve (grey, black) and kinematic invariants (blue) for $V/V_c = 0.3$ and K_d value indicated in Fig. 8(a)) (panel a), and for $V/V_c = 0.8$ with K_d corresponding with T (panel b) and $2T$ (panel c) parametric resonance (see Fig. 8(b)). The solid black line indicates the primary dispersion curve, and the green line indicates that of the non-periodic system. Red circles indicate intersections between the primary dispersion curve and kinematic invariants

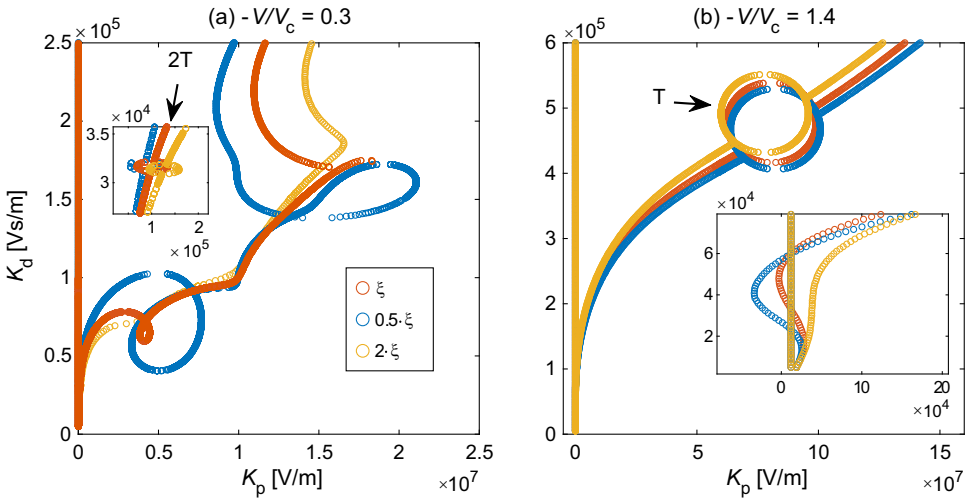

Fig. 11 Stability boundaries of the weakly periodic system for different magnitudes of the viscous-damping ratio ζ and for two values of the relative speed V/V_c

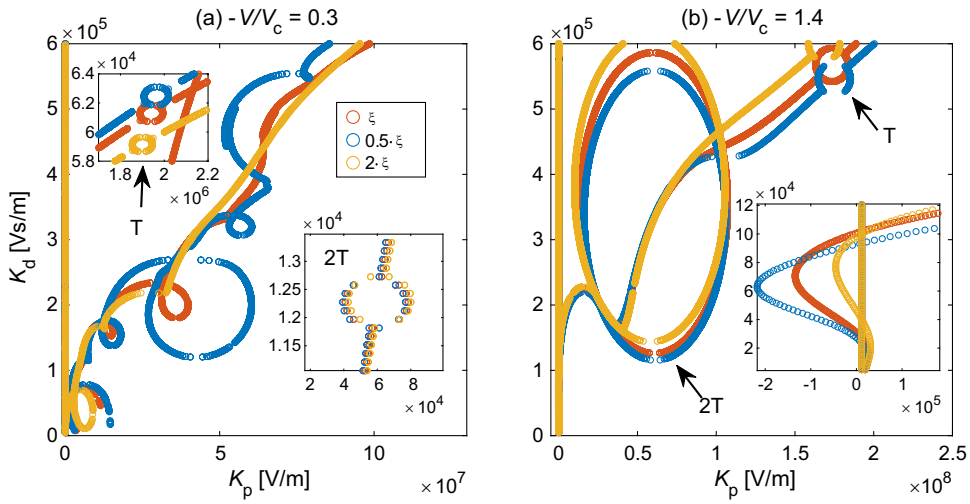

Fig. 12 Stability boundaries of the strongly periodic system for different magnitudes of the viscous-damping ratio ζ and for two values of the relative speed V/V_c

ings underline the importance of proper assessment of the damping in the guideway for the stability analysis.

8 Conclusions

The current study addresses the dynamic stability of a moving mass suspended electromagnetically from a flexible beam that is supported periodically by discrete elastic springs, with focus on the influence of the periodic nature of the supports and of the vehicle speed. The stability is governed by the wave induced and electromagnetic instability mechanisms, and each of them is related to a potentially destabilizing force: the controlled electromagnetic force and the reaction force of the guideway (i.e., the beam-foundation system). The former is destabilizing if the control is inappropriate, and the latter is destabilizing if sufficiently energetic anomalous Doppler waves are excited in the guideway (which feedback energy into the vehicle vibration). The overall stability is determined by the interaction of the two forces.

The system of equations governing the stability problem contains essentially one linear PDE and two linear ODEs, and all of them have time-periodic coefficients resulting from the periodically varying steady state defined by the original nonlinear equations of motion (i.e., nonlinearity in the contact force and in Kirchoff's law). The paper presents a method to find the stability boundary in the plane of control gains K_p, K_d of the PD controller that operates on the air gap; this simple controller has been chosen to facilitate comparison of the findings with those of the equivalent non-periodic system, with distributed support [37]. Formulated based on Floquet's theorem, the method searches for quasi-periodic free oscillations of the field variables, which is a generalization of Hill's method as the fundamental frequency of vibration Ω is generally unknown a priori. Employing a semi-analytical solution for the response of the periodically supported beam to a moving oscillatory force, the equations can be reformulated to an eigenvalue problem that can be solved straightforwardly, giving the combinations of K_p, K_d and Ω for which quasi-periodic free vibrations can exist. Connecting all points in the K_p, K_d plane and employing a transient analysis for validation, stable and unstable zones are identified, and with that the actual stability boundary.

The stability boundary obtained is roughly triangular, like for the equivalent non-periodic system. The left, straight boundary, which is even exactly the same, marks the emergence of a divergence instability. The right boundary generally marks the emergence of an oscillatory (flutter-type) instability, but specific, elliptical indentations are related to parametric resonances. The divergence instability is always electromagnetics induced, but the oscillatory instability and parametric resonances can be either wave induced or electromagnetics induced, as revealed by an energy analysis; it should be noted, however, that the encountered parametric resonances are mostly electromagnetics induced. Wave-induced instability takes place mostly for large speeds and only for small K_p, K_d, like for the non-periodic system. The right stability boundary locally bends back reducing the size of the stable zone considerably and cutting it essentially into two parts. Next to the elliptical indentations related to T and $2T$ parametric resonances, the latter being more pronounced, the right boundary has a significant amorphous indentation compared to that of the non-periodic system. The $2T$ parametric resonance ellipse is very significant in size compared to the width of the stable domain when the periodic inhomogeneity of the guideway is relatively strong.

The amorphous indentation is related to the occurrence of an evanescent wave in the periodic guideway. In that situation, there is less radiation damping compared to the non-periodic guideway (that predicts a propagating wave for the same parameters), which explains why the stable domain is more narrow. When the parametric resonance is electromagnetics induced, a standing wave may exist in the guideway, but that is certainly not generally the case. To get more insight into the relation between parametric resonance and the (energetic) wave types excited in the guideway, a dedicated in-depth energy analysis would be required, preferably for a guideway without damping. That analysis may also reveal when (e.g., at what speed) anomalous Doppler waves become more powerful than the regular Doppler waves to render the guideway's reaction force destabilizing.

Although the current study is fundamental in nature and the adopted model is perhaps too simplistic for detailed design, the findings do pave the way towards the design of safe and cost-effective Maglev and Hyperloop infrastructure as well as of electromagnetic-suspension controllers. The guideway should preferably be designed such that wave-induced instability does not occur in the operational speed range, or it should be counteracted by an effective controller. Furthermore, even if the instability is electromagnetics induced, the periodic nature of the guideway still significantly affects the shape of the stability boundary (i.e., parametric-resonance and amorphous indentations), which implies that detailed modeling of the guideway is in fact always necessary for stability assessment. Note that, for infrastructure and controller design, the aeroelastic instability mechanism must be incorporated too (next to the electromagnetics-induced and wave-induced mechanisms; see Sect. 1) as it influences the stability of Maglev and Hyperloop vehicles, particularly at high speeds. Including a realistic amount of damping in the guideway is also important, as shown in the current paper.

Finally, we emphasize that the wave-induced instability mechanism addressed in this paper, and more generally speaking the influence of the periodic guideway, is also relevant in the context of other (more advanced) control strategies

[34] as well as for different Maglev and Hyperloop suspension/levitation systems such as the electrodynamic, the hybrid and the superconducting magnet suspensions [5, 59–61]. How effective other control strategies/suspensions are in suppressing the wave-induced instability mechanism and the different instability types (e.g., parametric resonance) remains an open question.

Appendix A

In this appendix, we present the derivation of the steady-state response of an infinite, periodically supported (with discrete springs) beam to a moving harmonic load with arbitrary frequency $\bar{\omega}$ and amplitude F, which is used for steady-state response of the nonlinear system (Eq. (8)) as well as for the stability analysis (Eqs. (33) and (34)). The derivation is similar to that of Hoang et al. [48], but it is extended to the case of $\bar{\omega} \neq 0$. The response is governed by the following equation of motion:

$$\rho A \frac{\partial^2 w}{\partial t^2} + EI \frac{\partial^4 w}{\partial x^4} + \sum_{p=-\infty}^{\infty} R_p(t)\delta(x - pL) = F\mathrm{e}^{\mathrm{i}\bar{\omega}t}\delta(x - Vt), \tag{A1}$$

where $R_p(t)$ is the reaction force exerted by support p:

$$R_p(t) = k_\mathrm{s} w(x = pL, t). \tag{A2}$$

Following Belotserkovskiy [62], the periodicity condition for the reaction forces can be obtained, which in the time and frequency (ω) domains reads as follows (Fourier transform over time defined with $\mathrm{e}^{-\mathrm{i}\omega t}$):

$$R_p(t) = R(t - pT)\mathrm{e}^{\mathrm{i}\bar{\omega}pT}, \tag{A3}$$

$$\hat{R}_p(\omega) = \hat{R}(\omega)\mathrm{e}^{-\mathrm{i}(\omega-\bar{\omega})pT}, \tag{A4}$$

where $R(t)$ denotes the support reaction at $p = 0$, the hat signifies that the variable is defined in the frequency domain, and $T = L/V$.

To solve the problem, the Fourier transform is applied to Eq. (A1) over time and space (the latter is defined with $\mathrm{e}^{\mathrm{i}k_x x}$). An algebraic equation is obtained, which can be solved straightforwardly [48], resulting in

$$\tilde{w}(k_x, \omega) = \frac{2\pi}{EI}\frac{1}{D(k_x, \omega)}\left(\frac{F}{V}\delta(\kappa_0 - k_x) - \frac{\hat{R}}{L}\sum_{p=-\infty}^{\infty}\delta(\kappa_p - k_x)\right), \tag{A5}$$

where $\kappa_p = (\omega - \bar{\omega} - \omega_p)/V$, $D(\omega, k_x) = k_x^4 - \beta^4$ with $\beta^4 = \rho A\omega^2/EI$, and the tilde signifies that the variable is defined in the frequency-wavenumber domain. Clearly, $\hat{R}$ is still unknown, but an expression for it can be found using Eq. (A2) for $p = 0$ (note that $R_0 = R$) written in the frequency domain:

$$\hat{R} = k_\mathrm{s}\hat{w}(x = 0, \omega). \tag{A6}$$

To this end, the inverse Fourier transform over k_x is first evaluated to find the response in the frequency domain. The result reads

$$\hat{w}(x, \omega) = \frac{1}{EI}\frac{1}{V}\frac{\mathrm{e}^{-\mathrm{i}\kappa_0 x}}{D(\kappa_0, \omega)}F - \frac{1}{EI}\frac{1}{L}\sum_{p=-\infty}^{\infty}\frac{\mathrm{e}^{-\mathrm{i}\kappa_p x}}{D(\kappa_p, \omega)}\hat{R}. \tag{A7}$$

Substituting $x = 0$, we find

$$\hat{w}(x = 0, \omega) = \frac{F}{\hat{k}_{\mathrm{b,F}}} - \frac{\hat{R}}{\hat{k}_{\mathrm{b,R}}}, \tag{A8}$$

where, following [48],

$$\hat{k}_{\mathrm{b,F}} = EI\,V\,D(\kappa_0, \omega), \tag{A9}$$

$$\hat{k}_{\mathrm{b,R}} = \left(\frac{1}{EI}\frac{1}{L}\sum_{p=-\infty}^{\infty}\frac{1}{D(\kappa_p, \omega)}\right)^{-1} = 4EI\beta^3\left(\frac{\sin(\beta L)}{\cos(\beta L) - \cos(\kappa_0 L)} - \frac{\sinh(\beta L)}{\cosh(\beta L) - \cos(\kappa_0 L)}\right)^{-1}. \tag{A10}$$

Secondly, combining Eqs. (A6) and (A8), the expression for $\hat{R}$ is found:

$$\hat{R} = \hat{\alpha}F, \quad \hat{\alpha} = \frac{1}{\hat{k}_{\mathrm{b,F}}}\frac{k_\mathrm{s}\hat{k}_{\mathrm{b,R}}}{k_\mathrm{s} + \hat{k}_{\mathrm{b,R}}}. \tag{A11}$$

The time-domain response of the beam under the moving load is now found by evaluating the inverse Fourier integral over ω. By combining terms, we obtain

$$w(x = Vt, t) = \frac{1}{2\pi}\int_{-\infty}^{\infty}\hat{w}(x = Vt, \omega)\mathrm{e}^{\mathrm{i}\omega t}\,d\omega = F\sum_{p=-\infty}^{\infty}\gamma_p\mathrm{e}^{\mathrm{i}(\bar{\omega}+\omega_p)t}, \tag{A12}$$

where $\gamma_p = \gamma_p(\bar{\omega}, V) = \chi\delta_{0p} - \eta_p$ and

$$\chi = \frac{1}{2\pi}\frac{1}{EI}\frac{1}{V}\int_{-\infty}^{\infty}\frac{1}{D\left(\kappa_0,\omega\right)}\,d\omega, \tag{A13}$$

$$\eta_p = \frac{1}{2\pi}\frac{1}{EI}\frac{1}{L}\int_{-\infty}^{\infty}\frac{\hat{\alpha}}{D\left(\kappa_p,\omega\right)}\,d\omega. \tag{A14}$$

The expression in Eq. (A12) clearly shows that the response below the moving point load is quasi-periodic in time and contains the harmonic oscillation directly induced by the load itself as well as many other harmonics induced by the periodicity of the system. The integrals in the expressions for χ and η_p can only be taken numerically provided that some viscous/material damping is introduced into the model; otherwise, the poles of the integrands lie on the real ω axis. Note that for the case of $\bar{\omega} = 0$ and $p = 0$ (i.e., $\omega_p = 0$) the integrals in Eqs. (A13) and (A14) should be taken together to avoid a singularity at $\omega = 0$ in both integrands; the singularity is related to a non-physical, unconstrained rigid-body movement, and it can be verified that it vanishes when the integrands are combined.

The expression presented in Eq. (A12) is used in Sect. 3 for the steady-state response of the beam to a moving constant load; in that case $\bar{\omega} = 0$, $F = Mg$ and $\gamma_p(\bar{\omega} = 0, V) = c_p$ (see Eq. (8)). Equation (A12) is also used in Sect. 5 for the response of the beam to a moving harmonic load with frequency $\bar{\omega}_k$; see Eq. (33). In that case, $\bar{\omega} = \bar{\omega}_k$, $F = F_k$, $p = l$ and $\gamma_l(\bar{\omega}_k, V) = h_{kl}$; eventually, the index k is summed over as many harmonic forcing components are considered, as shown in Eq. (34).

Finally, we note that by combining the Eqs. (A8) and (A11), the following expression can be obtained for the frequency-domain response, written solely in terms of F:

$$\hat{w}(x = 0, \omega) = \frac{\hat{k}_{\mathrm{b,R}}}{\hat{k}_{\mathrm{b,F}}}\frac{1}{k_{\mathrm{s}} + \hat{k}_{\mathrm{b,R}}}F. \tag{A15}$$

The denominator $k_{\mathrm{s}} + \hat{k}_{\mathrm{b,R}}$ of the resulting expression, when equated to zero, gives precisely the intersections of the dispersion curves [55] of the periodically supported beam with the so-called kinematic invariants; the latter express the frequency-wavenumber content of the moving load and can be found from the arguments of the Dirac functions in Eq. (A5): $\omega = \bar{\omega} + \omega_p + k_x V$. The intersections provide the frequencies (ω) of the waves that are excited in the beam (and lead to peaks in the amplitude spectrum of $\hat{w}(x = 0, \omega)$). This justifies that the intersections of the dispersion curves with the kinematic invariants are considered in Sect. 7 when determining the waves excited in the guideway.

Author Contributions All authors contributed to the study conception and design. Material preparation, data collection and analysis were performed mostly by Rens J. van Leijden, Karel N. van Dalen and Andrei B. Fărăgău. The first draft of the manuscript was written by Karel N. van Dalen and all authors commented on previous versions of the manuscript. All authors read and approved the final manuscript.

Funding The authors express sincere gratitude to the European Union's Horizon Europe programme for its support through the Marie Skłodowska-Curie grant of Jithu Paul, project number 101106482 (HySpeed project).

Data Availability Relevant codes and data will be deposited at the international data repository 4TU.ResearchData (https://data.4tu.nl/) once the paper has been accepted.

Declarations

Conflict of interest The authors declare no Conflict of interest.

References

1. Gkoumas, K.: Hyperloop academic research: a systematic review and a taxonomy of issues. Appl. Sci. (2021). https://doi.org/10.3390/app11135951
2. Premsagar, S., Kenworthy, J.: A critical review of Hyperloop (ultra-high speed rail) technology: urban and transport planning, technical, environmental, economic, and human considerations. Front. Sustain. Cities. (2022). https://doi.org/10.3389/frsc.2022.842245
3. Museros, P., Lázaro, C., Pinazo, B., Monleón, S.: Key aspects in the analysis and design of Hyperloop™ infrastructure under static, dynamic and thermal loads. Eng. Struct. **239**, 112177 (2021). https://doi.org/10.1016/j.engstruct.2021.112177
4. Noland, J.K.: Prospects and challenges of the Hyperloop transportation system: a systematic technology review. IEEE Access **9**, 28439–28458 (2021). https://doi.org/10.1109/ACCESS.2021.3057788
5. Han, H.-S., Kim, D.-S.: Magnetic Levitation. Springer Tracts on Transportation and Traffic. Springer, Dordrecht (2016). https://doi.org/10.1007/978-94-017-7524-3
6. Dong, F., Hao, L., Park, D., Iwasa, Y., Huang, Z.: On the future sustainable ultra-high-speed Maglev: an energy-economical superconducting linear thrusting system. Energy Convers. Manag. **291**, 117247 (2023). https://doi.org/10.1016/j.enconman.2023.117247
7. Long, Z., Wang, Z., Zhaia, M., Li, X.: High-Speed Maglev Train's Levitation and Guidance Control, 1st edn. Advances in High-Speed Rail Technology. Springer, Singapore (2024). https://doi.org/10.1007/978-981-97-2309-6
8. Huang, H., Li, H., Sun, Y., Hu, X.: Development and challenges of Maglev transportation. In: Mohebbi, M. (ed.) Railway Transport and Engineering. IntechOpen, Rijeka (2024). Chap. 4. https://doi.org/10.5772/intechopen.1007211

9. Lee, H.-W., Kim, K.-C., Lee, J.: Review of Maglev train technologies. IEEE Trans. Magn. **42**(7), 1917–1925 (2006). https://doi.org/10.1109/TMAG.2006.875842
10. Cai, Y., Chen, S.S., Rote, D.M., Coffey, H.T.: Vehicle/guideway dynamic interaction in Maglev systems. J. Dyn. Syst. Meas. Contr. **118**(3), 526–530 (1996). https://doi.org/10.1115/1.2801176
11. Zhou, D., Hansen, C.H., Li, J., Chang, W.: Review of coupled vibration problems in EMS Maglev vehicles. Int. J. Acoust. Vib. **15**(1), 10–23 (2010). https://doi.org/10.20855/ijav.2010.15.1255
12. Inoue, T., Ishida, Y.: Nonlinear forced oscillation in a magnetically levitated system: the effect of the time delay of the electromagnetic force. Nonlinear Dyn. **52**(1), 103–113 (2008). https://doi.org/10.1007/s11071-007-9263-9
13. Zhang, L., Huang, L., Zhang, Z.: Stability and Hopf bifurcation of the Maglev system with delayed position and speed feedback control. Nonlinear Dyn. **57**(1–2), 197–207 (2009). https://doi.org/10.1007/s11071-008-9432-5
14. Popp, K., Schiehlen, W.: Ground Vehicle Dynamics, 1st edn. Springer, Berlin, Heidelberg (2010). https://doi.org/10.1007/978-3-540-68553-1
15. Paul, J., van Dalen, K.N., Fărăgău, A.B., van Leijden, R.J., Ouggaâli, M., Metrikine, A.V.: Suppressing parametric resonance of a Hyperloop vehicle using a parametric force. Phys. Rev. E **111**(3), 034210 (2025). https://doi.org/10.1103/PhysRevE.111.034210
16. Den Hartog, J.P.: Mechanical Vibrations, 4th edn. McGraw-Hill, New York (1956)
17. Xiao-Hui, Z., He-Mu, S., Han, W.: Nonlinear dynamic responses of high-speed railway vehicles under combined self-excitation and forced excitation considering the influence of unsteady aerodynamic loads. Nonlinear Dyn. **105**(4), 3025–3060 (2021). https://doi.org/10.1007/s11071-021-06795-4
18. Denisov, G.G., Kugusheva, E.K., Novikov, V.V.: On the problem of the stability of one-dimensional unbounded elastic systems. J. Appl. Math. Mech. **49**(4), 533–537 (1985). https://doi.org/10.1016/0021-8928(85)90065-6
19. Metrikine, A.V., Dieterman, H.A.: Instability of vibrations of a mass moving uniformly along an axially compressed beam on a viscoelastic foundation. J. Sound Vib. **201**(5), 567–576 (1997). https://doi.org/10.1006/jsvi.1996.0783
20. Mazilu, T., Dumitriu, M., Tudorache, C.: On the dynamics of interaction between a moving mass and an infinite one-dimensional elastic structure at the stability limit. J. Sound Vib. **330**(15), 3729–3743 (2011). https://doi.org/10.1016/j.jsv.2011.02.026
21. Metrikine, A.V., Popp, K.: Instability of vibrations of an oscillator moving along a beam on an elastic half-space. Eur. J. Mech. A. Solids **18**(2), 331–349 (1999). https://doi.org/10.1016/S0997-7538(99)80020-5
22. Mazilu, T.: Interaction between moving tandem wheels and an infinite rail with periodic supports - green's matrices of the track method in stationary reference frame. J. Sound Vib. **401**, 233–254 (2017). https://doi.org/10.1016/j.jsv.2017.04.035
23. Stojanović, V., Petković, M.D.: Dynamic stability of vibrations and critical velocity of a complex bogie system moving on a flexibly supported infinity track. J. Sound Vib. **434**, 475–501 (2018). https://doi.org/10.1016/j.jsv.2017.07.057
24. Zhao, M., de Oliveira Barbosa, J.M., Yuan, J., Metrikine, A.V., van Dalen, K.N.: Instability of vibrations of an oscillator moving at high speed through a tunnel embedded in soft soil. J. Sound Vib. **494**, 115776 (2021). https://doi.org/10.1016/j.jsv.2020.115776
25. Dimitrovová, Z.: On the critical velocity of moving force and instability of moving mass in layered railway track models by semi-analytical approaches. Vibration **6**(1), 113–146 (2023). https://doi.org/10.3390/vibration6010009
26. Wu, H., Zeng, X.H., Yu, Y.: Motion stability of high-speed Maglev systems in consideration of aerodynamic effects: a study of a single magnetic suspension system. Acta Mech. Sinica **33**, 1084–1094 (2017). https://doi.org/10.1007/s10409-017-0698-z
27. Wu, H., Zeng, X.-H., Gao, D.-G., Lai, J.: Dynamic stability of an electromagnetic suspension Maglev vehicle under steady aerodynamic load. Appl. Math. Model. **97**, 483–500 (2021). https://doi.org/10.1016/j.apm.2021.04.008
28. Huang, Z.-D., Kong, W.-K., Wang, S.-M., Zhou, Z.-B., Ni, Y.-Q., Chang, N.: Dynamic and stability analysis of high-speed Maglev train-guideway coupled system under crosswind. J. Sound Vib. **609**, 119092 (2025). https://doi.org/10.1016/j.jsv.2025.119092
29. Yau, J.D.: Vibration control of Maglev vehicles traveling over a flexible guideway. J. Sound Vib. **321**(1), 184–200 (2009). https://doi.org/10.1016/j.jsv.2008.09.030
30. Shi, J., Wang, Y.: Dynamic response analysis of single-span guideway caused by high speed Maglev train. Lat. Am. J. Solids Struct. **8**(3), 1–14 (2011). https://doi.org/10.1590/S1679-78252011000300001
31. Li, J.-H., Li, J., Zhou, D.-F., Yu, P.-C.: Self-excited vibration problems of Maglev vehicle-bridge interaction system. J. Central South Univ. **21**(11), 4184–4192 (2014). https://doi.org/10.1007/s11771-014-2414-5
32. Kim, K.-J., Han, J.-B., Han, H.-S., Yang, S.-J.: Coupled vibration analysis of Maglev vehicle-guideway while standing still or moving at low speeds. Veh. Syst. Dyn. **53**(4), 587–601 (2015). https://doi.org/10.1080/00423114.2015.1013039
33. Hu, J., Ma, W., Chen, X., Luo, S.: Levitation stability and Hopf bifurcation of EMS Maglev trains. Math. Probl. Eng. **2020**, 1–12 (2020). https://doi.org/10.1155/2020/2936838
34. Sun, Y., Li, F., Wang, Y., Zhao, X., Wu, J., Rao, Z., Guo, W., Lin, G.: A survey of coupled vibration characteristics and control methods in maglev transportation: challenges, methods and progress. J. Railw. Sci. Technol. **1**, 1–27 (2025). https://doi.org/10.1016/j.jrst.2025.10.002
35. Schneider, G., Schmid, P., Dignath, F., Eberhard, P.: Modeling and simulation of a high-speed Maglev vehicle on an infinite elastic guideway. In: ECCOMAS Thematic Conference on Multibody Dynamics (2021). https://doi.org/10.3311/ECCOMASMBD2021-161 . ECCOMAS Thematic Conference on Multibody Dynamics
36. Fărăgău, A.B., Wang, R., Metrikine, A.V., van Dalen, K.N.: The interplay between the electro-magnetic and wave-induced instability mechanisms in the Hyperloop transportation system. In: Lacarbonara, W. (ed.) Advances in Nonlinear Dynamics, Volume I, pp. 617–627. Springer, Cham (2024). https://doi.org/10.1007/978-3-031-50631-4_52
37. Fărăgău, A.B., Metrikine, A.V., Paul, J., van Leijden, R., van Dalen, K.N.: Controlling instability of high-speed magnetically suspended vehicles: the interaction of the electromagnetic and wave-induced instability mechanisms. J. Sound Vib. **608**, 119077 (2025). https://doi.org/10.1016/j.jsv.2025.119077
38. Vesnitskii, A.I., Metrikin, A.V.: Parametric instability in the oscillations of a body moving uniformly in a periodically inhomogeneous elastic system. J. Appl. Mech. Tech. Phys. **34**(2), 266–271 (1993). https://doi.org/10.1007/BF00852523
39. Verichev, S.N., Metrikine, A.V.: Instability of vibrations of a mass that moves uniformly along a beam on a periodically inhomogeneous foundation. J. Sound Vib. **260**(5), 901–925 (2003). https://doi.org/10.1016/S0022-460X(02)00936-7
40. Metrikine, A.V.: Parametric instability of a moving particle on a periodically supported infinitely long string. J. Appl. Mech. **75**(1), 011006 (2008). https://doi.org/10.1115/1.2745368
41. Abe, K., Chida, Y., Balde Quinay, P.E., Koro, K.: Dynamic instability of a wheel moving on a discretely supported infinite rail. J. Sound Vib. **333**(15), 3413–3427 (2014). https://doi.org/10.1016/j.jsv.2014.03.027

42. Cai, Y., Chen, S.S., Mulcahy, T.M., Rote, D.M.: Dynamic stability of Maglev systems. Technical Report ANL-92/21, Argonne National Laboratory, Argonne, IL (1992)
43. Yabuno, H., Seino, T., Yoshizawa, M., Tsujioka, Y.: Dynamical behavior of a levitated body with magnetic guides: parametrically excitation of the subharmonic type due to the vertical motion of levitated body. JSME Int. J. Ser. 3, Vib. Control Eng. Eng. Ind. **32**(3), 428–435 (1989). https://doi.org/10.1299/jsmec1988.32.428
44. Sun, Z.: Moving-inertial-loads-induced dynamic instability for slender beams considering parametric resonances. J. Vib. Acoust. **138**(1), 011014 (2015). https://doi.org/10.1115/1.4031518
45. Gao, H., Yang, B.: Parametric vibration of a flexible structure excited by periodic passage of moving oscillators. J. Appl. Mech. **87**(7), 071001 (2020). https://doi.org/10.1115/1.4046781
46. Gao, H., Yang, B.: Dynamic response of a beam structure excited by sequentially moving rigid bodies. Int. J. Struct. Stab. Dyn. **20**(8), 2050093 (2020). https://doi.org/10.1142/S0219455420500935
47. Han, J.-B., Han, H.-S., Lee, J.-M., Kim, S.-S.: Dynamic modeling and simulation of EMS Maglev vehicle to evaluate the levitation stability and operational safety over an elastic segmented switch track. J. Mech. Sci. Technol. **32**(7), 2987–2998 (2018). https://doi.org/10.1007/s12206-018-0602-1
48. Hoang, T., Duhamel, D., Foret, G., Yin, H.P., Joyez, P., Caby, R.: Calculation of force distribution for a periodically supported beam subjected to moving loads. J. Sound Vib. **388**, 327–338 (2017). https://doi.org/10.1016/j.jsv.2016.10.031
49. de Oliveira Barbosa, J.M., van Dalen, K.N.: Dynamic response of an infinite beam periodically supported by sleepers resting on a regular and infinite lattice: semi-analytical solution. J. Sound Vib. **458**, 276–302 (2019). https://doi.org/10.1016/j.jsv.2019.06.014
50. Nayfeh, A.H.: Nonlinear Oscillations. Wiley, New York (1979). Reprint edition
51. Païdoussis, M.P.: Fluid-Structure Interactions: Slender Structures and Axial Flow, vol. 1. Academic Press, San Diego (1998)
52. de Oliveira Barbosa, J.M., Fărăgău, A.B., van Dalen, K.N.: A lattice model for transition zones in ballasted railway tracks. J. Sound Vib. **494**, 115840 (2021). https://doi.org/10.1016/j.jsv.2020.115840
53. Metrikine, A.V.: Unstable vertical oscillations of an object moving uniformly along an elastic guide as a result of an anomalous Doppler effect. Acoust. Phys. **40**(1), 85–89 (1994)
54. van Leijden, R.J.: Parametric instability of an oscillator moving on a railway track. Master's thesis, Delft University of Technology, Faculty of Civil Engineering and Geosciences (2021). https://resolver.tudelft.nl/uuid:7054fa71-0f6a-4f96-8069-c0ea877f6763
55. Nordborg, A.: Vertical rail vibrations: pointforce excitation. Acustica **84**, 280–288 (1998)
56. Mead, D.M.: Wave propagation in continuous periodic structures: research contributions from southampton, 1964–1995. J. Sound Vib. **190**(3), 495–524 (1996). https://doi.org/10.1006/jsvi.1996.0076
57. Lu, T., Yuan, S., Wang, T., Liu, X., Wang, P., Chen, R.: Dynamic response and wave motion of a periodically supported beam under an ultra-high-speed load: wave dispersion and critical velocities. Int. J. Solids Struct. **291**, 112694 (2024). https://doi.org/10.1016/j.ijsolstr.2024.112694
58. Fărăgău, A.B., de Oliveira Barbosa, J.M., Metrikine, A.V., van Dalen, K.N.: Dynamic amplification in a periodic structure with a transition zone subject to a moving load: three different phenomena. Math. Mech. Solids **27**(9), 1740–1760 (2022). https://doi.org/10.1177/10812865221094318
59. Long, Z., He, G., Xue, S.: Study of EDS & EMS hybrid suspension system with permanent-magnet halbach array. IEEE Trans. Magn. **47**(12), 4717–4724 (2011). https://doi.org/10.1109/TMAG.2011.2159237
60. Huang, H., Deng, Z., Zhang, X., Cheng, Y., Hong, Y., Li, H.: Numerical simulation and parameter identification of dynamic levitation force of HTS pinning Maglev for engineering application. J. Supercond. Novel Magn. **34**(11), 2753–2760 (2021). https://doi.org/10.1007/s10948-021-06042-2
61. Fu, Y., Li, H., Wang, L., Zhang, P., Zhang, K., Deng, Z.: Dynamic simulation of HTS Maglev vehicle/track coupled based on discrete elastic support track model. Phys. C Supercond. it Appl. **592**, 1353997 (2022). https://doi.org/10.1016/j.physc.2021.1353997
62. Belotserkovskiy, P.M.: On the oscillations of infinite periodic beams subjected to a moving concentrated force. J. Sound Vib. **193**(3), 705–712 (1996). https://doi.org/10.1006/jsvi.1996.0309